
Article:
Johnson, Brian S., Zhao, Ying-Tao, Fasolino, Maria et al. (10 more authors) (2017) Biotin tagging of MeCP2 in mice reveals contextual insights into the Rett syndrome transcriptome. Nature Medicine. pp. 1203-1214. ISSN 1078-8956

https://doi.org/10.1038/nm.4406

Biotin tagging of MeCP2 in mice reveals contextual insights into the Rett syndrome transcriptome

B.S. Johnson[1†], Y.T. Zhao[1†], M. Fasolino[1†], J.M. Lamonica[1], Y.J. Kim[2], G. Georgakilas[1], K.H. Wood[1], D. Bu[1], Y. Cui[1], D. Goffin[1], G. Vahedi[1], T.H. Kim[2], Z. Zhou[1*]

Affiliations:

[1]Department of Genetics, University of Pennsylvania Perelman School of Medicine, Philadelphia, Pennsylvania 19104, USA

[2]Department of Biological Sciences and Center for Systems Biology, The University of Texas at Dallas, Richardson, Texas 75080, USA

[†]These authors contributed equally to this work.

[*]To whom correspondence should be addressed: zhaolan@mail.med.upenn.edu

Abstract:

Mutations in *MECP2* cause Rett syndrome (RTT), an X-linked neurological disorder characterized by regressive loss of neurodevelopmental milestones and acquired psychomotor deficits. However, the cellular heterogeneity of the brain impedes an understanding of how *MECP2* mutations contribute to RTT. Here we developed a Cre-inducible method for cell type-specific biotin tagging of MeCP2 in mice. Combining this approach with an allelic series of knockin mice carrying frequent RTT mutations (T158M and R106W) enabled the selective profiling of RTT-associated nuclear transcriptomes in excitatory and inhibitory cortical neurons. We found that most gene expression changes are largely specific to each RTT mutation and cell type. Lowly expressed cell type-enriched genes are preferentially disrupted by MeCP2 mutations, with upregulated and downregulated genes reflecting distinct functional categories. Subcellular RNA analysis in MeCP2 mutant neurons further reveals reductions in the nascent transcription of long genes and uncovers widespread post-transcriptional compensation at the cellular level. Finally, we overcame X-linked cellular mosaicism in female RTT models and identified distinct gene expression changes between neighboring wild-type and mutant neurons, altogether providing contextual insights into RTT etiology that support personalized therapeutic interventions.

Introduction

RTT is a progressive X-linked neurological disorder that represents one of the most common causes of intellectual disability among young girls. Patients experience a characteristic loss of acquired social and psychomotor skills and develop stereotyped hand movements, breathing irregularities, and seizures after 6-18 months of normal development[1]. Approximately 95% of RTT cases are mapped to the X-linked gene encoding methyl-CpG binding protein 2 (MeCP2), a ubiquitously expressed protein that is highly enriched in postmitotic neurons[2,3]. The majority of RTT-associated mutations cluster within two functionally distinct domains of MeCP2. The Methyl-CpG Binding Domain (MBD) allows MeCP2 to bind to methylated cytosines[4]. The Transcriptional Repression Domain (TRD) mediates protein-protein interactions with histone deacetylase-containing co-repressors, such as the NCoR-SMRT and mSin3A complexes[5–7]. These domains support MeCP2 as a chromatin factor that mediates transcriptional repression[7,8], although transcriptional activation by MeCP2 is also reported[9–11].

Different mutations in *MECP2*, together with random X-chromosome inactivation (XCI), underlie a spectrum of clinical severity in RTT patients[12]. Among the most frequent RTT mutations, three are missense mutations in the MeCP2 MBD, including R106W (2.76% of RTT patients), R133C (4.24%), and T158M (8.79%)[13]. Typical RTT patients bearing the R133C mutation display milder clinical symptoms, whereas patients carrying the T158M or R106W mutation exhibit moderate or severe symptoms, respectively[12]. Although the clinical severity of these mutations scales with their effects on MeCP2 binding affinity to methylated DNA[14–17], this relationship is not fully understood on a molecular level. Mouse models carrying RTT mutations can recapitulate this phenotypic variability, but most studies are limited to hemizygous male mice[17–21]. Despite that RTT predominantly affects heterozygous females, an experimental

strategy to selectively identify gene expression changes from *Mecp2* mutant-expressing cells in a mosaic female brain has not yet been developed.

Given that MeCP2 is a chromatin-bound nuclear protein, the identification of MeCP2 transcriptional targets in the brain remains key towards illuminating RTT etiology[22]. However, target identification is confounded by the cellular heterogeneity of the brain, which contains multiple intermixed cell types that differ in morphology, function, electrophysiological properties, and transcriptional programs[23–25]. Analyses using heterogeneous brain tissues obscure cell type-specific gene expression changes, impeding the assessment of MeCP2 function at the transcriptional level[26]. The identification of transcriptional targets is further complicated by the widespread binding patterns of MeCP2 to methylated cytosines (mCpG and mCpA)[8,27,28] or unmethylated GC-rich regions[29] throughout the genome.

In this study, we addressed the confounding effects of cellular heterogeneity by engineering genetically modified mice whereby MeCP2 is labeled with biotin using Cre-Lox recombination. To understand the molecular impact of RTT mutations on cell type-specific gene expression *in vivo*, we also developed an allelic series of knockin mice bearing one of two frequent RTT missense mutations, T158M and R106W. When combined with Fluorescence-Activated Cell Sorting (FACS), this strategy allows for the isolation of neuronal nuclei from targeted cell types, effectively circumventing cellular heterogeneity in the mouse brain and X-linked mosaicism in female mice. Our findings support a contextualized model by which cell autonomous and non-autonomous transcriptional changes in different cell types contribute to the molecular severity of neuronal deficits in RTT, providing new directions for therapeutic development.

Results

Engineering a System to Genetically Biotinylate MeCP2 *In Vivo*: Biotin-mediated affinity tagging has been widely utilized in cell and animal models for multiple experimental approaches because of the strong (K_d = 4x10^{-14}M) and specific interaction between biotin and avidin protein[30]. We exploited this approach to investigate MeCP2 function by using homologous recombination to insert a short 23-amino acid affinity tag immediately upstream of the *Mecp2* stop codon (Fig. 1a and Supplementary Fig. 1a). This tag comprises a TEV protease cleavage site and a 15-amino acid biotinylation consensus motif (termed Tavi, *T*EV and *Avi*din-binding) that can be post-translationally labeled with biotin by the *E. coli* biotin ligase, BirA. To biotinylate the tag in cell types of interest, we also generated Cre-dependent BirA transgenic mice (herein *R26*^{cBirA}; Supplementary Fig. 1b). Therefore, upon crossing these mice to a cell type-specific Cre line, BirA is expressed and subsequently biotinylates MeCP2-Tavi (Fig. 1b). We used *EIIa-Cre*[31] to ubiquitously express BirA (*R26*^{BirA}) and confirmed that MeCP2 is specifically biotinylated *in vivo* only when BirA is expressed and the Tavi tag is present (Fig. 1c and Supplementary Fig. 1c).

To examine the possibility that tagging MeCP2 adversely affects its function, we assessed MeCP2 expression levels, DNA binding, and protein-protein interactions in 20-week old *Mecp2*$^{Tavi/y}$ (herein TAVI) and littermate *Mecp2*$^{+/y}$ (WT) mice. We found that total MeCP2 protein, but not RNA, is significantly reduced by ~40% in TAVI mice, and a similar trend towards ~40% reduction is also observed among soluble and chromatin-bound protein fractions (Supplementary Fig. 1d-f). However, Tavi-tagged and untagged MeCP2 both exhibit comparable levels of chromatin binding at high and low affinity genomic sites, including highly methylated

major satellite repeats and IAP elements, and MeCP2-Tavi remains associated with the NCoR-SMRT co-repressor (Supplementary Fig. 1g-h). Although a 50% reduction in MeCP2 expression is sufficient to cause hypoactivity and subtle behavioral phenotypes in mice[32], TAVI mice appear similar to WT mice and do not display overt RTT-like features using phenotypic scoring[33] over an observational period of 20 weeks (Fig. 1g-j, Supplementary Fig. 1i, and data not shown/B.S.J).

MeCP2 Missense Mutations Recapitulate RTT-like Phenotypes in Mice: To examine the molecular relationship between MeCP2 affinity for methylated DNA and phenotypic severity, we generated independent *Mecp2*$^{T158M\text{-}Tavi}$ (herein T158M) and *Mecp2*$^{R106W\text{-}Tavi}$ (R106W) knock-in mice in parallel with TAVI mice (Fig. 1a). Relative to TAVI controls, we found that T158M and R106W mice both display a ~70-80% reduction in MeCP2 protein expression despite equivalent levels of mRNA at 6 weeks of age (Fig. 1e, Supplementary Fig. 1j), similar to other mouse models bearing MeCP2 MBD mutations[17,18,21]. However, there is a trend towards relatively higher MeCP2 protein levels in T158M than R106W mice across development (Supplementary Fig. 2a). Immunofluorescent (IF) staining of hippocampal sections from T158M and R106W mice revealed diffusely distributed MeCP2 throughout the nucleus that accompanied a loss of localization to heterochromatic foci, supporting the impaired binding of mutant MeCP2 to mCpGs *in vivo* (Fig. 1d). Streptavidin IF, which is noticeably lower in *Mecp2* mutant mice, also confirmed a loss of mutant MeCP2 localization to heterochromatic foci and further illustrated a redistribution of mutant MeCP2 to the nucleolus (Fig. 1d and Supplementary Fig. 2b-c), a property reminiscent of GFP-tagged MeCP2 lacking its MBD[34].

Using sub-nuclear fractionation, we confirmed that a greater proportion of MeCP2 T158M or R106W protein occupies the soluble fraction when compared to WT or TAVI protein (Supplementary Fig. 2d), consistent with the loss of chromatin binding in mutant mice (Fig. 1d). By further extracting chromatin-bound MeCP2 with different salt concentrations, we found that MeCP2 R106W is more readily released at lower salt concentrations (200mM NaCl) than MeCP2 WT, TAVI, or T158M protein, suggesting that MeCP2 R106W has the lowest binding affinity for chromatin (Fig. 1f and Supplementary Fig. 2e). Phenotypic comparisons revealed that T158M and R106W mice both exhibit RTT-like features similar to that of *Mecp2*-null mice, including decreased brain and body weight, and an age-dependent increase in phenotypic score (Fig. 1g-i). Although lifespan is significantly reduced in all three *Mecp2* mutant mice, the median survival of R106W mice more closely resembles that of *Mecp2*-null than T158M mice (Fig. 1j). Both mutations demonstrated a significant difference in survival curves (T158M median survival = 14 weeks; R106W median survival = 10 weeks; Mantel Cox $P = 0.012$). Together, these data suggest that T158M and R106W mutations represent a partial and complete loss-of-function, respectively.

Genetic Biotinylation Permits Cell Type-specific Transcriptional Profiling: We next devised a biotinylation-based strategy for cell type-specific nuclei isolation and transcriptional profiling (Fig. 2a-b). We used the *NeuroD6/NEX-Cre* line[35] to drive BirA expression and MeCP2-Tavi biotinylation in forebrain excitatory neurons (Fig. 2a and Supplementary Fig. 3a-g). Quantification of pan-neuronal (NeuN), pan-inhibitory (GAD67), and inhibitory-specific (parvalbumin, somatostatin and calretinin) neuronal markers in the somatosensory cortex of $Mecp2^{Tavi/y}$;$R26^{cBirA/+}$;$NEX^{Cre/+}$ (herein NEX-Cre) mice demonstrated that biotinylation occurs in

~80% of NeuN+ cortical neurons devoid of inhibitory markers (Supplementary Fig. 3h). FACS using stained cortical nuclei from NEX-Cre mice identified three distinct nuclear populations (Fig. 2c). RT-PCR for cell type-specific markers confirmed that NeuN+Biotin+ nuclei reflect excitatory neurons, whereas NeuN+Biotin- nuclei represent a mixture of inhibitory interneuron subtypes (Fig. 2c-d). Astrocytic, microglial and oligodendrocytic markers are restricted to the third, non-neuronal population of NeuN-Biotin- nuclei (Fig. 2c-d). We also used the Dlx5/6-Cre line[36] to drive BirA expression in forebrain GABAergic neurons and obtained results inverse to that of NEX-Cre (Fig. 2a and Supplementary Fig. 3a-j), confirming that MeCP2-Tavi is reliably biotinylated in Cre-defined cell types.

Because MeCP2 is known to modulate transcription[22], nuclear RNA-seq would afford an unique opportunity to study the primary effects of RTT mutations on gene expression. We thus performed transcriptional profiling in 6-week old male mice near the onset of RTT-like phenotypes. We employed the NEX-Cre driver and isolated cortical excitatory and inhibitory nuclei from T158M, R106W and TAVI mice via FACS, followed by total RNA-seq (Supplementary Table 1). Biological replicates were well-correlated (Fig. 2e), and ~74% of total reads mapped to introns, serving as a proxy for chromatin-associated transcriptional activity[37,38]. Unsupervised hierarchical clustering shows that replicate transcriptomes from cortical excitatory and inhibitory neurons in TAVI mice are highly correlated by cell type, and genic-mapped reads illustrate selectively expressed genes in each cell type (Fig. 2e-f and Supplementary Fig. 4a). We identified 9,379 differentially expressed genes (DEGs, FDR < 0.05) between excitatory and inhibitory neurons, the majority (86.9%) of which comprise protein-coding genes (Table 1 and Supplementary Fig. 4b). Among the protein-coding fraction of cell type-enriched DEGs, 3,958 genes (0.15 – 4.70 fold change) display Gene Ontology (GO) functions consistent with

glutamatergic pyramidal cell types (EXC-enriched; Supplementary Fig. 4c), whereas the remaining 4,194 genes (0.17 – 7.77 fold change) exhibit GO functions consistent with metabolically active GABAergic interneurons (INH-enriched; Supplementary Fig. 4d).

Protein-Coding Genes are More Severely Affected in R106W Mice: We next compared nuclear gene expression profiles in excitatory and inhibitory neurons between mutant (T158M, R106W) and control (TAVI) mice to identify and characterize DEGs associated with the appearance of RTT-like phenotypes (Fig. 3a). We identified more DEGs in excitatory and inhibitory neurons of R106W than T158M mice, indicating that the number of misregulated genes positively scales with the severity of the *Mecp2* mutation (Fig. 3b and Table 1). More than 90% of MeCP2 DEGs are protein-coding genes (Supplementary Fig. 5a), significantly higher than the percentage of protein-coding genes in the genome (60.4%), or among actively expressed (77.7-78.3%) and cell type-enriched (86.2-87.7%) genes (Supplementary Fig. 4b). We therefore excluded non-coding genes from further analyses. We note that the number and percentage of protein-coding DEGs overlapping between T158M and R106W genotypes is greater in inhibitory (107 genes) than excitatory neurons (69 genes). Moreover, overlapping DEGs tend to be misregulated in the same direction (Fig. 3c).

The median fold change of T158M and R106W DEGs is small in mutant neurons compared to overall differences in gene expression between excitatory and inhibitory neurons (Supplementary Fig. 5b and Table 1). We further compared fold changes between T158M and R106W DEGs, limiting our analysis to protein-coding genes that overlap between genotypes to account for disproportionate numbers of DEGs. Within this subset, we found that the median fold change among upregulated and downregulated DEGs is consistently higher in both cell

types of R106W mice than those of T158M mice (Fig. 3c), consistent with a more severe phenotype in R106W mice.

Transcriptional Features of T158M and R106W DEGs: We next compared MeCP2 DEGs across excitatory and inhibitory neurons and found limited overlap between the two cell types (6.2% of T158M DEGs, 10.7% of R106W DEGs; Fig. 3d), indicating that most DEGs reflect cell type-specific transcriptional changes. Indeed, EXC/INH-enriched genes are significantly overrepresented among MeCP2 DEGs in each cell type, comprising ~70-80% of genes (Fig. 3e and Table 1). Moreover, EXC- and INH-enriched genes are preferentially downregulated and upregulated, respectively, in each cell type (Fig. 3e and Supplementary Fig. 5c).

We next performed a pre-ranked Gene Set Enrichment Analysis (GSEA, FDR < 0.1) to determine whether upregulated and downregulated DEGs represent functionally distinct categories. Upregulated DEGs in T158M and R106W mice are both primarily associated with transcriptional regulation. These include DNA-binding transcriptional activators, repressors, and chromatin remodelers, most of which tend to be INH-enriched genes (Fig. 3f and Supplementary Fig. 5d). Significant functional categories associated with downregulated DEGs, however, are specifically detected in R106W excitatory neurons and enriched for post-synaptic membrane proteins, including various ion channels, synaptic scaffolding proteins, and ionotropic glutamate receptors (Fig. 3f). Although significant gene functions were not identified among downregulated DEGs in inhibitory neurons using our GSEA FDR cutoff, gene functions associated with upregulated DEGs in R106W inhibitory neurons are related to cellular metabolism and signal transducer activity (Supplementary Fig. 5e).

Upon examining the relative expression levels of MeCP2 DEGs using Fragments Per Kilobase of transcript per Million mapped reads (FPKM), we noticed that T158M, R106W, and overlapping DEGs display significantly lower FPKM values relative to total expressed genes in each cell type (Fig. 3g). To exclude the possibility of gene filtering biases associated with RNA-seq, we randomly selected 12 low-expressing DEGs that overlap between both mutations and independently measured their primary and mature RNA transcripts in excitatory neuronal nuclei using RT-PCR (Supplementary Table 2). We found that 10 out of 12 genes show significant gene expression changes that resemble those using RNA-seq (83.3% positive validation rate; Supplementary Fig. 6a-b), confirming that genes with low transcriptional activity are indeed affected by MeCP2 mutations. To examine whether lowly expressed genes are selectively enriched for MeCP2 DEGs, we binned actively expressed genes from each cell type into four percentiles (Q1-Q4) according to expression level. EXC- and INH-enriched genes served as reference distributions across percentiles for each cell type (Supplementary Fig. 6c). In comparison, T158M and R106W DEGs are preferentially enriched in Q1, the bottom 25th percentile of actively expressed genes, in both excitatory and inhibitory neurons (Fisher Exact one-tailed *P*, T158M: EXC = 1.11e-07, INH = 2.03e-04; R106W: EXC = 4.04e-08, INH = 1.50e-02; Supplementary Fig. 6c). Between the two mutations, T158M DEGs are more likely to be lowly expressed than R106W DEGs (Fisher Exact Odds Ratio (OR) for Q1, T158M: EXC = 3.1, INH = 3.2; R106W: EXC = 2.0, INH = 1.3; Supplementary Fig. 6c). Accordingly, R106W-specific DEGs have significantly higher FPKM values than T158M DEGs in both cell types and are predominantly downregulated in R106W neurons (Fig. 3g and Supplementary Fig. 6d). This preferential downregulation of high-expressing genes appears consistent with the specific loss of synaptic gene functions in R106W excitatory neurons (Fig. 3f-g and Supplementary Fig. 6d).

Subcellular RNA Pools Reveal Global Transcriptional and Post-transcriptional Changes: Two recent reports implicate MeCP2 in the transcriptional repression of long genes, which are preferentially upregulated in the neurons of multiple RTT models[27,39]. We therefore examined the possibility that genome-wide transcriptional changes may correlate with T158M and R106W phenotypic and molecular severity. Similar to those studies, we sorted and binned expressed protein-coding genes according to gene length and measured the mean fold change in *Mecp2* mutant neurons. Notably, nuclear transcriptomes revealed a striking inversion of previously reported gene expression changes whereby short (≤ 100kb in gene length) and long (> 100kb in gene length) genes trend towards upregulation and downregulation, respectively, in a length-dependent manner (Supplementary Fig. 7a).

Although most nuclear RNAs comprise intron-containing pre-mRNA transcripts on chromatin, the presence of processed mRNA transcripts awaiting nuclear export may potentially confound the assessment of transcriptional events[40]. We therefore performed global nuclear run-on with high-throughput sequencing (GRO-seq[41]) to directly assess *de novo* transcriptional activity by RNA polymerase in cortical nuclei of TAVI and R106W mice. Similar to sorted nuclear RNA, the nascent transcription of short and long genes in R106W neurons is predominantly increased and decreased, respectively (Fig. 4a). LOESS local regression of DEGs that were identified in R106W excitatory and inhibitory neurons also revealed a similar overall trend towards the preferential downregulation of long genes (Fig. 4a). The genome-wide trend we observe in sorted nuclear RNA thus represents a primary effect at the transcriptional level, prompting us to further investigate if the length-dependent upregulation of long genes that was previously reported may represent an indirect effect of MeCP2-dependent transcriptional

deregulation. To test this, we resected cortical tissue from TAVI and R106W mice, and subjected each cortical half to whole cell or nuclear RNA isolation in parallel, followed by sequencing. Cortical whole cell RNA from mutant mice displayed a length-dependent increase in the mean expression of long genes (Fig. 4b), similar to what was previously described[27,39]. In contrast, cortical nuclear RNA isolated from the same TAVI and R106W mice exhibited a length-dependent upregulation of short genes and downregulation of long genes (Fig. 4c), corroborating the transcriptional changes we observed from nascent RNA (Fig. 4a) and nuclear RNA from sorted nuclei (Supplementary Fig. 7a). Using the 10,390 expressed genes associated with *de novo* transcription by GRO-seq (Fig. 4d), we observed that genes upregulated in nascent and nuclear RNA pools are cumulatively shorter in length relative to those upregulated in whole cell RNA, and the inverse was observed among downregulated genes (Fig. 4e). Thus, gene expression changes in *Mecp2* mutant neurons appear to be substantially different between subcellular compartments.

To directly compare individual genes across subcellular compartments, we next classified all 10,390 expressed genes into eight subgroups that reflect the total number of arrangements by which a gene can be misregulated across three given RNA pools ($2^3 = 8$). Groups B and D comprise 38.4% of expressed genes which are involved in neuronal projection and cellular stress, respectively, and represent expression changes that are misregulated in the same direction across nascent, nuclear, and whole cell RNA pools (Fig. 4f and Supplementary Fig. 7b). Among these groups of genes, $\log_2$ fold changes measured from the whole cell are significantly smaller than that in the nuclear compartment, suggesting that gene expression changes in the nucleus are post-transcriptionally minimized in the cell (Fig. 4f and Supplementary Fig. 7c). The majority of genes (48%), however, exhibit expression changes in nascent RNAs that are reversed in the

whole cell compartment (Groups A,C,G,H; Fig. 4f). Groups A and C consist of relatively long, EXC-enriched genes that are transcriptionally downregulated in nascent RNA but post-transcriptionally upregulated in whole cell RNA (Fig. 4f and Supplementary Fig. 7d-e). DAVID gene ontology revealed that Group A genes are associated with synaptic functions and intracellular signaling (Fig. 4g). Groups G and H consist of considerably shorter, INH-enriched genes that are transcriptionally upregulated in nascent RNA but post-transcriptionally downregulated in whole cell RNA (Fig. 4f and Supplementary Fig. 7d-e), and Group G genes are functionally associated with cellular energy and metabolism in mitochondria (Fig. 4g). RT-PCR validation of primary and mature RNA transcripts for several genes from Groups A/C, B, and D recapitulated these apparent expression differences between subcellular compartments, particularly when genes were analyzed as a collective in their respective Group (Fig. 4h, Supplementary Fig. 8 and Supplementary Table 2). Notably, upon analyzing *de novo* transcriptional activity derived from GRO-seq for genes expressed in sorted excitatory or inhibitory neurons (Supplementary Fig. 7f), we found a trend towards long genes being more severely downregulated in both cell types bearing the R106W mutation than the T158M mutation (Fig. 4i and Supplementary Fig. 7g), consistent with a more severe phenotype in R106W mice.

To gain insight into the apparent switch in gene misregulation between subcellular compartments, we next used publically available HITS-CLIP datasets from the mouse brain to examine genes whose transcripts are typically bound and regulated by RNA-binding proteins (RBPs), and tested for associations with distinct subcellular gene expression changes in *Mecp2* mutant neurons. K-means clustering of 10,390 cortically expressed genes across HITS-CLIP data for 12 RBPs (MBNL1-2, TDP43, FUS, TAF15, FMR1, HuR, APC, RBFOX1-3, and AGO2)

311 identified 5 major gene clusters (Supplementary Fig. 9a). We found one subset of genes whose
312 transcripts display significantly higher levels of HuR binding, but lower levels of AGO2 binding
313 (RBP Clusters 1 and 4), and another subset showing significantly higher levels of AGO2 binding
314 but lower levels of HuR binding (RBP Clusters 2, 3 and 5; Supplementary Fig. 9b-c). HuR binds
315 to the 3'UTR of mRNA transcripts (Supplementary Fig. 9d) and is known to increase mRNA
316 stability[42]. Conversely, AGO2 functions to promote mRNA degradation through AGO2-bound
317 miRNAs[43]. Both HuR and AGO2 genes are also actively expressed in neurons at 6-weeks of age
318 (Supplementary Fig. 9e). By comparing gene Groups A-H, which summarize subcellular gene
319 expression changes in *Mecp2* mutant neurons (Fig. 4f), to functionally-distinct RBP clusters
320 (Supplementary Fig. 9a-c), we found that many downregulated nascent RNA transcripts from
321 Groups A, B, and C are significantly associated with RBP Clusters 1 and 4 and are post-
322 transcriptional targets of HuR (Supplementary Fig. 9f). By contrast, upregulated nascent RNA
323 transcripts in *Mecp2* mutant neurons, particularly from Groups G and H, show associations with
324 RBP Clusters 2, 3, and 5, and are targets of AGO2-bound miRNAs (Supplementary Fig. 9f). The
325 opposite functions of HuR and AGO2 in the post-transcriptional regulation of mRNA stability
326 likely alter the abundance of cellular RNAs in a group- or cluster-specific manner. Therefore,
327 gene expression differences between subcellular compartments in *Mecp2* mutant mice could be
328 post-transcriptionally mediated in part by RBPs (Supplementary Fig. 9g).
329
330 **Female RTT Mouse Models Reveal Cell and Non-Cell Autonomous DEGs:** RTT is an X-
331 linked disorder that primarily affects heterozygous females. However, the extent to which
332 intermixed *Mecp2* WT and mutant (MUT) neurons in cellular mosaic RTT females affect each
333 other at the level of gene expression remains unknown. The reduced expression level of T158M

and R106W mutant protein allowed us to use the same tagging and sorting strategy in male mice to isolate and profile WT (denoted by subscript: $T158M_{WT}$, $R106W_{WT}$) and MUT ($T158M_{MUT}$, $R106W_{MUT}$) cells from mosaic female mice. These include TAVI (*Mecp2*$^{Tavi/+}$;*R26*$^{cBirA/+}$;*NEX*$^{Cre/+}$), T158M (*Mecp2*$^{Tavi/T158M\text{-}Tavi}$;*R26*$^{cBirA/+}$;*NEX*$^{Cre/+}$), and R106W (*Mecp2*$^{Tavi/R106W\text{-}Tavi}$;*R26*$^{cBirA/+}$;*NEX*$^{Cre/+}$) heterozygous females that each carry a Tavi-tagged WT allele and a Tavi-tagged T158M, R106W, or untagged WT allele. Upon aging these mice to ~18 weeks, when T158M and R106W females both exhibit RTT-like phenotypes (Fig. 5a), cortical excitatory nuclei were isolated for FACS (Fig. 5b-c and Supplementary Fig. 10a). From the number of females sampled, we did not detect skewed XCI (> 75%) among excitatory neurons in TAVI, T158M, or R106W mice (Fig. 5d).

By comparing the gene expression profiles of WT or MUT neurons from heterozygous mutant mice to those from control mice ($TAVI_{WT}$), a total of 526 and 678 unique protein-coding DEGs in $T158M_{WT\ and\ MUT}$ and $R106W_{WT\ and\ MUT}$ neurons were identified, respectively (Fig. 5e, Supplementary Fig. 10b and Table 1). Most DEGs represent cell autonomous gene expression changes that occur in mutant neurons alone (Fig. 5e). However, a larger proportion of R106W DEGs are also found in $R106W_{WT}$ neurons (43.4%; Fig. 5e), revealing a mutation-specific susceptibility of WT neurons to non-cell autonomous gene expression changes in heterozygous females. Using principal component analysis (PCA) to plot the first two major axes of transcriptome variation, we found that PC2 separates neuronal populations by *Mecp2* allele status (WT vs. MUT neurons) irrespective of the T158M or R106W mutation (Fig. 5f), indicating that *Mecp2* mutations induce cell autonomous changes that are transcriptionally distinct from neighboring wild-type neurons. However, PC1 accounts for nearly twice the variation as PC2 and clusters $R106W_{WT\ and\ MUT}$ populations away from other genotypes, likely

due to the extensive number of indirect DEGs associated with this mutation. In contrast, against PC1 and PC2, $T158M_{WT}$ neurons closely resemble $TAVI_{WT}$ (Fig. 5f), indicating that the non-cell autonomous DEGs observed in $R106W_{WT}$ neurons specifically arise due to the increased severity of R106W mutation in $R106W_{MUT}$ neurons.

We further found 194 DEGs that overlap between T158M and R106W female mice, most of which are misregulated in the same direction (Fig. 5g). Among these genes, cell autonomous transcriptional changes (149 genes, 76.8%) are more likely to be shared across independent *Mecp2* mutations than non-cell autonomous changes (9 genes, 4.6%; Fig. 5h). These overlapping DEGs also show higher fold changes in R106W than T158M female mice, but this difference is mainly driven by indirect DEGs in R106W neurons (Fig. 5i).

In R106W female mice, we found that non-cell autonomous DEGs are predominantly upregulated (~60%) in contrast to cell autonomous DEGs (~48%; Supplementary Fig. 10b), and display significantly higher fold changes than cell autonomous DEGs (Supplementary Fig. 10c). Furthermore, cell autonomous DEGs are considerably longer in gene length, specifically among upregulated genes (Supplementary Fig. 10d). To determine if cell and non-cell autonomous DEGs represent distinct biological processes, we also performed pre-ranked GSEA (FDR < 0.1) and found that non-cell autonomous gene expression changes primarily affect cell-to-cell signaling and negative regulation of protein phosphorylation (Supplementary Fig. 10e). These DEGs include several immediate early and late response genes that are induced by neuronal activity and modulate signaling pathways associated with synaptic plasticity[44]. In contrast, cell autonomous DEGs are significantly associated with transcriptional regulation (Supplementary Fig. 10f). These functional categories demonstrate a marked resemblance to those observed in excitatory neurons of male T158M and R106W mice (Fig. 5j). The striking consistency with

which these functional annotations characterize *Mecp2* mutant neurons, despite apparent differences in age and sex, supports the cell autonomous disruption of these functions as a key, contributing factor to RTT pathogenesis.

Discussion: The complexity of MeCP2 molecular function, coupled with the cellular heterogeneity of the brain, confounds the study of transcriptional changes in RTT. We thus combined *in vivo* biotinylation with Cre-Lox technology to label both wild-type and mutant MeCP2 from different neuronal populations and examined RTT-associated transcriptomes in mice. Notably, the 23AA Tavi tag can be readily used to target any given protein using CRISPR-Cas9 technology[45] for cell type-specific biochemical purifications, molecular profiling, and imaging applications.

By using an allelic series of RTT mutations to perform a transcriptome analysis of cortical neurons, we identified similarities and differences in gene expression features that couple impairments in MeCP2's ability to bind DNA to RTT phenotypic severity. We found that lowly-expressed, cell type-enriched genes are sensitive to the effects of both T158M and R106W mutations, which likely contributes to the specificity of MeCP2-mediated gene expression changes among different neuronal cell types. Both mutations also display conserved transcriptional features among upregulated DEGs in male and female neurons, which include genes encoding INH-enriched transcription factors and chromatin remodelers. The upregulation of transcriptional regulators could contribute to the shared RTT etiology between T158M and R106W mice, as well as the genome-wide trend towards increased transcription of shorter, INH-enriched genes associated with cellular respiration and energy metabolism. This provides

402 transcriptional insight into clinical features among both mildly and severely affected RTT
403 patients that resemble mitochondrial and metabolic disorders[46].

404 However, the greater impairment in MeCP2 R106W binding to neuronal chromatin
405 associates with increased RTT phenotypic severity, and notably correlates with the larger
406 number and degree of misregulated genes that are more highly expressed and predominately
407 downregulated relative to the T158M mutation. These transcriptional differences extend to most
408 long genes throughout the genome, which are highly expressed in neurons[47]. Our datasets are in
409 partial agreement with global reductions in Ser5-phosphorylated RNA polymerase in *Mecp2*-null
410 neuronal nuclei[48], supporting MeCP2 as a global modulator of gene transcription. Loss of
411 MeCP2 occupancy may either alter local chromatin organization, which could decrease the
412 efficiency of transcriptional elongation[49] and lead to the downregulation of long genes, or may
413 abrogate HDAC3-mediated recruitment of transcription factors required for long gene
414 transcriptional activation[50]. Because downregulated genes associate with synaptic morphology
415 and function, and R106W mice have reduced lifespans compared to T158M mice, reductions in
416 long gene transcription may act as modifiers to worsen RTT-like phenotypes. RTT patients with
417 mutations that preserve MeCP2 binding do exhibit milder features than patients for whom
418 binding is disrupted[12]. Transcriptional assessments with mutations preserving MeCP2 binding
419 are thus necessary to further refine these genotype-phenotype correlations.

420 Because MeCP2 is a DNA-binding nuclear protein[22], nuclear and nascent RNA pools
421 provide additional insights into the primary effects of RTT mutations on transcriptional
422 activity[37,38,51] that complement the reported whole cell upregulation of long genes in RTT[27,39].
423 Whole cell RNA is subject to post-transcriptional regulation[40,52,53], being notably enriched for
424 cytoplasmic mRNAs that are bound by various RBPs to modulate their steady-state abundance

and turnover. We found that many downregulated nascent RNA transcripts are targets of HuR, which increases mRNA stability in the brain[42] and may post-transcriptionally upregulate these transcripts in whole cell RNA. Upregulated nascent RNA transcripts tend to associate with miRNA-bound AGO2, which may post-transcriptionally mitigate their upregulation by increasing rates of mRNA decay[43]. These post-transcriptional mechanisms may abate cellular consequences arising from global alterations in synaptic, mitochondrial, and metabolic gene transcription. Whole cell gene expression changes in RTT may thus be compensatory and not entirely representative of transcriptional activity, questioning the therapeutic benefit of decreasing long gene transcription for treating RTT. Identifying RBPs that contribute to cellular compensation may yield a novel class of interventional therapies administered prior to or during the initial phases of RTT, minimizing its pathological impact.

Finally, our approach allows for the molecular profiling of mosaic neurons from female mice that represent accurate preclinical RTT models, revealing non-cell autonomous changes in WT neurons that depend on mutation severity. However, to better elucidate direct and indirect contributions to RTT, further investigation requires examination of females with a wide range of XCI ratios across multiple ages, cell types, and *Mecp2* mutations. Non-cell autonomous DEGs include genes induced by neuronal activity to reduce synaptic responsiveness to excessive neuronal stimuli[44]. Nuclear RNA transcripts of two late-response genes in particular, *Bdnf* and *Igf1*, were found to be transcriptionally upregulated in WT and MUT neuronal nuclei of 18-week old R106W female mice. As *Bdnf* and *Igf1* encode neuroprotective peptides that ameliorate RTT symptoms[20], the selective upregulation of non-cell autonomous DEGs in R106W mice may be a protective response to increased neuronal activity or stress among severely affected mosaic neurons. Currently, BDNF and IGF-1 peptides are being tested in clinical trials[54,55]. Further study

of molecular pathways associated with non-cell autonomous DEGs may thus reveal additional RTT therapeutic targets and avenues.

Data availability: All sequencing data reported in this study has been deposited in the NCBI Gene Expression Omnibus (GSE83474). Mouse lines generated from this study have been deposited at The Jackson Laboratory (Bar Harbor, ME) under the following stock numbers: *R26*^{cBirA} (Stock #030420), *Mecp2*^{Tavi} (Stock #030422), *Mecp2*$^{T158M\text{-}Tavi}$ (Stock #029642), and *Mecp2*$^{R106W\text{-}Tavi}$ (Stock #029643).

Acknowledgements: We would like to thank the IDDRC Mouse Gene Manipulation Core at Children's Hospital Boston (U54HD090255, M. Thompson), the Gene Targeting Core (P01DK049210, K. Kaestner) and the Transgenic and Chimeric Mouse Facility (J. Richa) at University of Pennsylvania for help in generating transgenic mice, the Flow Cytometry and Cell Sorting Resource Laboratory (H. Pletcher, W. DeMuth), and the Next Generation Sequencing Core (J. Schug) for technical assistance. B.S.J. is supported by a Cell and Molecular Biology Training Grant (TG32GM072290) and the UNCF/Merck Graduate Research Dissertation Fellowship. This work is supported by NIH grants K22AI112570 (G. V.), R21AI107067 and R01CA140485 (T.H.K.), R01MH091850 and R01NS081054 (Z.Z.), and a basic research grant from Rettsyndrome.org (Z.Z.). Z.Z is a Pew Scholar in the Biomedical Sciences.

Author Contributions: Conceptualization, B.S.J. and Z.Z.; Methodology, B.S.J., J.M.L., D.G., and Z.Z.; Investigation, B.S.J., Y.T.Z., M.F., J.M.L., K.H.W., Y.J.K., and D.B.; Formal Analyses, B.S.J., Y.T.Z., G.G., and T.H.K.; Validation, B.S.J., M.F., J.M.L., and G.V.;

Resources, B.S.J., Y.T.Z. and Y.C.; Data Curation, Y.T.Z.; Writing – Original Draft, B.S.J.; Writing – Review & Editing, B.S.J., Y.T.Z., M.F. and Z.Z.; Visualization, B.S.J.; Project Administration and Funding Acquisition, Z.Z.

Competing Financial Interest: The authors declare no competing financial interests.

References

1. Chahrour, M. & Zoghbi, H. Y. The story of Rett syndrome: from clinic to neurobiology. *Neuron* **56,** 422–37 (2007).
2. Amir, R. E. *et al.* Rett syndrome is caused by mutations in X-linked MECP2, encoding methyl-CpG-binding protein 2. *Nat. Genet.* **23,** 185–188 (1999).
3. Shahbazian, M. D., Antalffy, B., Armstrong, D. L. & Zoghbi, H. Y. Insight into Rett syndrome: MeCP2 levels display tissue- and cell-specific differences and correlate with neuronal maturation. *Hum. Mol. Genet.* **11,** 115–124 (2002).
4. Lewis, J. D. *et al.* Purification, sequence, and cellular localization of a novel chromosomal protein that binds to Methylated DNA. *Cell* **69,** 905–914 (1992).
5. Jones, P. L. *et al.* Methylated DNA and MeCP2 recruit histone deacetylase to repress transcription. *Nat. Genet.* **19,** 187–191 (1998).
6. Lyst, M. J. *et al.* Rett syndrome mutations abolish the interaction of MeCP2 with the NCoR/SMRT co-repressor. *Nat. Neurosci.* **16,** 898–902 (2013).
7. Nan, X. *et al.* Transcriptional repression by the methyl-CpG-binding protein MeCP2 involves a histone deacetylase complex. *Nature* **393,** 386–9 (1998).

8. Skene, P. J. *et al.* Neuronal MeCP2 Is Expressed at Near Histone-Octamer Levels and Globally Alters the Chromatin State. *Mol. Cell* **37,** 457–468 (2010).
9. Chahrour, M. *et al.* MeCP2, a Key Contributor to Neurological Disease, Activates and Represses Transcription. *Science* **320,** 1224–1229 (2008).
10. Chen, L. *et al.* MeCP2 binds to non-CG methylated DNA as neurons mature, influencing transcription and the timing of onset for Rett syndrome. *Proc. Natl. Acad. Sci.* **112,** 5509–5514 (2015).
11. Li, Y. *et al.* Global Transcriptional and Translational Repression in Human-Embryonic-Stem-Cell-Derived Rett Syndrome Neurons. *Cell Stem Cell* **13,** 446–458 (2013).
12. Cuddapah, V. A. *et al.* Methyl-CpG-binding protein 2 (MECP2) mutation type is associated with disease severity in Rett syndrome. *J. Med. Genet.* **51,** 152–158 (2014).
13. RettBASE: Rett Syndrome Variation Database. Available at: http://mecp2.chw.edu.au/. (Accessed: 8th April 2016)
14. Ghosh, R. P., Horowitz-Scherer, R. A., Nikitina, T., Gierasch, L. M. & Woodcock, C. L. Rett syndrome-causing mutations in human MeCP2 result in diverse structural changes that impact folding and DNA interactions. *J Biol Chem* **283,** 20523–34 (2008).
15. Ho, K. L. *et al.* MeCP2 Binding to DNA Depends upon Hydration at Methyl-CpG. *Mol. Cell* **29,** 525–531 (2008).
16. Ballestar, E., Yusufzai, T. M. & Wolffe, A. P. Effects of Rett syndrome mutations of the methyl-CpG binding domain of the transcriptional repressor MeCP2 on selectivity for association with methylated DNA. *Biochemistry (Mosc.)* **39,** 7100–7106 (2000).

17. Brown, K. *et al.* The molecular basis of variable phenotypic severity among common missense mutations causing Rett syndrome. *Hum. Mol. Genet.* ddv496 (2015). doi:10.1093/hmg/ddv496
18. Goffin, D. *et al.* Rett syndrome mutation MeCP2 T158A disrupts DNA binding, protein stability and ERP responses. *Nat Neurosci* **15,** 274–283 (2012).
19. Baker, S. A. *et al.* An AT-Hook Domain in MeCP2 Determines the Clinical Course of Rett Syndrome and Related Disorders. *Cell* **152,** 984–996 (2013).
20. Katz, D. M. *et al.* Preclinical research in Rett syndrome: setting the foundation for translational success. *Dis. Model. Mech.* **5,** 733–745 (2012).
21. Lamonica, J. M. *et al.* Elevating expression of MeCP2 T158M rescues DNA binding and Rett syndrome–like phenotypes. *J. Clin. Invest.* **127,** (2017).
22. Lyst, M. J. & Bird, A. Rett syndrome: a complex disorder with simple roots. *Nat. Rev. Genet.* **16,** 261–275 (2015).
23. Fishell, G. & Heintz, N. The Neuron Identity Problem: Form Meets Function. *Neuron* **80,** 602–612 (2013).
24. Molyneaux, B. J. *et al.* DeCoN: Genome-wide Analysis of In Vivo Transcriptional Dynamics during Pyramidal Neuron Fate Selection in Neocortex. *Neuron* **85,** 275–288 (2015).
25. Mo, A. *et al.* Epigenomic Signatures of Neuronal Diversity in the Mammalian Brain. *Neuron* **86,** 1369–1384 (2015).
26. Zhao, Y.-T., Goffin, D., Johnson, B. S. & Zhou, Z. Loss of MeCP2 function is associated with distinct gene expression changes in the striatum. *Neurobiol. Dis.* **59,** 257–266 (2013).

27. Gabel, H. W. *et al.* Disruption of DNA-methylation-dependent long gene repression in Rett syndrome. *Nature* **522,** 89–93 (2015).
28. Guo, J. U. *et al.* Distribution, recognition and regulation of non-CpG methylation in the adult mammalian brain. *Nat. Neurosci.* **17,** 215–222 (2014).
29. Rube, H. T. *et al.* Sequence features accurately predict genome-wide MeCP2 binding in vivo. *Nat. Commun.* **7,** 11025 (2016).
30. Malik, H. S. & Henikoff, S. A Simple Method for Gene Expression and Chromatin Profiling of Individual Cell Types within a Tissue. *Cell* **18,** 1030–1040 (2010).
31. Lakso, M. *et al.* Efficient in vivo manipulation of mouse genomic sequences at the zygote stage. *Proc. Natl. Acad. Sci. U. S. A.* **93,** 5860–5865 (1996).
32. Samaco, R. C. *et al.* A partial loss of function allele of Methyl-CpG-binding protein 2 predicts a human neurodevelopmental syndrome. *Hum. Mol. Genet.* **17,** 1718–1727 (2008).
33. Guy, J., Gan, J., Selfridge, J., Cobb, S. & Bird, A. Reversal of neurological defects in a mouse model of Rett syndrome. *Science* **315,** 1143–7 (2007).
34. Kumar, A. *et al.* Analysis of protein domains and Rett syndrome mutations indicate that multiple regions influence chromatin-binding dynamics of the chromatin-associated protein MECP2 in vivo. *J. Cell Sci.* **121,** 1128–1137 (2008).
35. Goebbels, S. *et al.* Genetic targeting of principal neurons in neocortex and hippocampus of NEX-Cre mice. *Genes. N. Y. N 2000* **44,** 611–621 (2006).
36. Monory, K. *et al.* The Endocannabinoid System Controls Key Epileptogenic Circuits in the Hippocampus. *Neuron* **51,** 455–466 (2006).

37. Bhatt, D. M. *et al.* Transcript Dynamics of Proinflammatory Genes Revealed by Sequence Analysis of Subcellular RNA Fractions. *Cell* **150,** 279–290 (2012).
38. Ameur, A. *et al.* Total RNA sequencing reveals nascent transcription and widespread co-transcriptional splicing in the human brain. *Nat. Struct. Mol. Biol.* **18,** 1435–1440 (2011).
39. Sugino, K. *et al.* Cell-Type-Specific Repression by Methyl-CpG-Binding Protein 2 Is Biased toward Long Genes. *J. Neurosci.* **34,** 12877–12883 (2014).
40. Maniatis, T. & Reed, R. An extensive network of coupling among gene expression machines. *Nature* **416,** 499–506 (2002).
41. Core, L. J., Waterfall, J. J. & Lis, J. T. Nascent RNA Sequencing Reveals Widespread Pausing and Divergent Initiation at Human Promoters. *Science* **322,** 1845–1848 (2008).
42. Brennan, C. M. & Steitz, J. A. HuR and mRNA stability. *Cell. Mol. Life Sci. CMLS* **58,** 266–277 (2001).
43. Höck, J. & Meister, G. The Argonaute protein family. *Genome Biol.* **9,** 210 (2008).
44. Flavell, S. W. & Greenberg, M. E. Signaling Mechanisms Linking Neuronal Activity to Gene Expression and Plasticity of the Nervous System. *Annu. Rev. Neurosci.* **31,** 563–590 (2008).
45. Yang, H. *et al.* One-Step Generation of Mice Carrying Reporter and Conditional Alleles by CRISPR/Cas-Mediated Genome Engineering. *Cell* **154,** 1370–1379 (2013).
46. Müller, M. & Can, K. Aberrant redox homoeostasis and mitochondrial dysfunction in Rett syndrome. *Biochem. Soc. Trans.* **42,** 959–964 (2014).
47. Zylka, M. J., Simon, J. M. & Philpot, B. D. Gene Length Matters in Neurons. *Neuron* **86,** 353–355 (2015).

48. Linhoff, M. W., Garg, S. K. & Mandel, G. A High-Resolution Imaging Approach to Investigate Chromatin Architecture in Complex Tissues. *Cell* **163,** 246–255 (2015).
49. King, I. F. *et al.* Topoisomerases facilitate transcription of long genes linked to autism. *Nature* **501,** 58–62 (2013).
50. Nott, A. *et al.* Histone deacetylase 3 associates with MeCP2 to regulate FOXO and social behavior. *Nat. Neurosci.* **advance online publication,** (2016).
51. Djebali, S. *et al.* Landscape of transcription in human cells. *Nature* **489,** 101–108 (2012).
52. Buxbaum, A. R., Yoon, Y. J., Singer, R. H. & Park, H. Y. Single-molecule insights into mRNA dynamics in neurons. *Trends Cell Biol.* **25,** 468–475 (2015).
53. Mauger, O., Lemoine, F. & Scheiffele, P. Targeted Intron Retention and Excision for Rapid Gene Regulation in Response to Neuronal Activity. *Neuron* **92,** 1266–1278 (2016).
54. Khwaja, O. S. *et al.* Safety, pharmacokinetics, and preliminary assessment of efficacy of mecasermin (recombinant human IGF-1) for the treatment of Rett syndrome. *Proc. Natl. Acad. Sci. U. S. A.* **111,** 4596–4601 (2014).
55. Lombardi, L. M., Baker, S. A. & Zoghbi, H. Y. MECP2 disorders: from the clinic to mice and back. *J. Clin. Invest.* **125,** 2914–2923 (2015).

Figure 1. Utilization and characterization of *Mecp2*^{Tavi} mice and associated RTT variants. **(a)** Diagram of wild-type and tagged MeCP2 showing R106W or T158M missense mutations. MBD, Methyl-CpG Binding Domain; TRD, Transcriptional Repression Domain. **(b)** Breeding strategy to biotinylate the Tavi tag in a Cre-dependent manner. **(c)** Representative western blot showing the conditions in which the Tavi tag is biotinylated using whole brain nuclear extracts. Blot is probed with streptavidin for biotin detection and antibodies against MeCP2 N-terminus, Tavi tag, and NeuN. **(d)** Representative images showing immunofluorescent detection of biotinylated MeCP2 and mutant variants in hippocampal sections of untagged (WT) and tagged (TAVI, T158M, R106W) male mice at 6 weeks of age. Tissue is probed with streptavidin for biotin detection and antibody against the MeCP2 C-terminus. Scale bars represent 10 μm. **(e)** Quantification and representative western blot comparing MeCP2 protein expression levels between TAVI and mutant (T158M, R106W) male mice at 6 weeks of age. Blot is probed with antibodies against the MeCP2 C-terminus and TBP ($n_{replicates}$ = 3, One-way ANOVA). **(f)** Quantification of salt-extracted MeCP2 from chromatin using 200mM (*left*) and 400mM (*right*) NaCl, normalized to extracts using 500mM NaCl (see Supplemental Fig. 2e; $n_{replicates}$ = 4-5, One-way ANOVA). **(g)** Box-and-whisker plot of brain weights from untagged (WT, KO (*Mecp2*-null)) and tagged (TAVI, T158M, R106W) male mice at 6 weeks of age (n_{WT} = 20, n_{TAVI} = 11, n_{KO} = 6, n_{T158M} = 6, n_{R106W} = 12; One-way ANOVA). Box limits denote 25th and 75th percentiles, center line denotes median, '+' denotes mean, and whiskers denote data max and min. Each genotype is indicated with a different color. **(h)** Body weight over postnatal age in untagged (WT, KO) and tagged (TAVI, T158M, R106W) male mice. Data points consist of at least 6 observations each. Total number of mice assessed: n_{WT} = 31, n_{TAVI} = 23, n_{KO} = 15, n_{T158M} = 14, n_{R106W} = 28. **(i)** RTT-like phenotypic score across postnatal development in untagged (WT, KO)

and tagged (TAVI, T158M, R106W) male mice. Data points over time consist of at least 6 observations each. Total number of mice assessed: $n_{WT} = 31$, $n_{TAVI} = 23$, $n_{KO} = 15$, $n_{T158M} = 14$, $n_{R106W} = 28$. **(j)** Kaplan-Meier survival curve for untagged (WT, KO) and tagged (TAVI, T158M, R106W) male mice ($n_{WT} = 31$, $n_{TAVI} = 23$, $n_{KO} = 17$, $n_{T158M} = 39$, $n_{R106W} = 26$). *$P < 0.5$, **$P < 0.01$, ***$P < 0.001$, ****$P < 0.0001$, n.s. = not significant; all pooled data depicts mean ± SEM unless otherwise stated. See also **Supplementary Figs. 1 and 2**.

Figure 2. Cell type-specific transcriptional profiling of neuronal nuclei. **(a)** Representative images showing immunofluorescent detection of biotinylated MeCP2-Tavi protein in Cre-specified neuronal populations of the mouse hippocampus. Probed using streptavidin for biotin detection and antibody against the MeCP2 C-terminus. Scale bars represent 100μm. **(b)** Schematic of cortical nuclei preparation and FACS isolation. **(c)** FACS analysis of labeled cortical nuclei populations. Data shown is representative of nine independent experiments using NEX-Cre mice. Percentages indicate the mean distribution of neurons that are NeuN+Biotin+ (excitatory; 85.2% ± 0.35) or NeuN+Biotin- (inhibitory; 14.8% ± 0.35). **(d)** RT-PCR validation of FACS-isolated populations depicted in (c) ($n_{replicates}$ = 3, Two-way ANOVA). **(e)** Pearson correlation of biological replicate nuclear RNA-seq libraries within (intra-replicate) and across (inter-replicate) FACS-isolated populations depicted in (c). Colors correspond to EXC-enriched (blue) and INH-enriched (red) genes identified through differential expression analysis of excitatory and inhibitory neurons. Note lower Pearson correlation and clear dispersal of cell type-enriched genes across FACS populations. **(f)** IGV browser snapshot of *Dlgap1* genomic locus in excitatory and inhibitory neurons of TAVI male mice at 6 weeks of age. RefSeq and Ensembl gene annotations are both shown. **P* < 0.5, ***P* < 0.01, ****P* < 0.001, *****P* < 0.0001, n.s. = not significant; all pooled data depicts mean ± SEM. See also **Supplementary Figs. 3 and 4**.

Figure 3. Analysis of T158M and R106W differentially expressed genes. **(a)** FACS isolation of cortical excitatory and inhibitory neuronal nuclei from TAVI, T158M, or R106W male mice at 6 weeks of age. **(b)** Total number of protein coding and non-coding differentially expressed genes (DEGs) identified in excitatory or inhibitory neurons of *Mecp2* mutant mice. **(c)** Heatmaps display $\log_2$ fold changes among protein-coding DEGs in excitatory and inhibitory neurons of *Mecp2* mutant mice, compared across genotypes. Excitatory DEGs $n_{shared} = 69$ genes, Hypergeometric $P = 3.15e^{-77}$. Inhibitory DEGs $n_{shared} = 107$ genes, Hypergeometric $P = 5.33e^{-134}$. Boxplots compare $\log_2$ median fold changes among overlapping DEGs between T158M and R106W neurons (One-tailed Wilcoxon Signed Rank). **(d)** Heatmap displaying $\log_2$ fold changes among protein-coding DEGs in excitatory and inhibitory neurons of *Mecp2* mutant mice, compared across cell types. **(e)** *Left graph*, Distribution of constitutive, EXC- or INH-enriched genes among T158M and R106W protein-coding DEGs, compared against genomic distribution (Chi-square Goodness-of-Fit). *Right graph,* Bar plot summarizing R106W DEGs in excitatory neurons, partitioned by cell type-enriched or constitutive genes, and which are preferentially upregulated or downregulated. Red indicates statistical significance (One-tailed Fisher's Exact Test). **(f)** Enrichment map of pre-ranked Gene Set Enrichment Analysis (GSEA) functional network associations. Data represents DEGs from R106W (top) and T158M (bottom) excitatory neurons (*P-value* < 0.01, *Q-value* < 0.1). Nodes denote functional categories, colored by Normalized Enrichment Score (NES). Line weight denotes extent of gene overlap between connected nodes. Red text highlights the similarity in functional annotations between both genotypes. **(g)** Boxplots comparing the $\log_2$ FPKM distribution of actively expressed genes against T158M, R106W, and shared DEGs for each cell type (Pairwise Wilcoxon Rank Sum *P*

displayed). *$P < 0.5$, **$P < 0.01$, ***$P < 0.001$, ****$P < 0.0001$, n.s. = not significant. See also **Supplementary Figs. 5 and 6**.

675

676 **Figure 4.** Genome-wide length-dependent transcriptional changes in RTT mutant mice. **(a)**
677 Genome-wide $\log_2$ fold changes in R106W mice (n = 2) compared to TAVI mice (n = 2) at 6
678 weeks of age using GRO-seq. *Top*, Lines represent mean fold change in expression for genes
679 binned according to gene length (200 gene bins, 40 gene step) as described in[27]. Ribbon
680 represents SEM of genes in each bin. *Bottom*, Smoothed scatterplot depicting LOESS correlation
681 between gene length and $\log_2$ fold change for all individual protein-coding genes detected in
682 GROseq. Genes in red highlight R106W DEGs identified from sorted excitatory and inhibitory
683 neuronal nuclei. **(b,c)** Same as in (a), but using total RNA-seq analysis of whole cell (b) or
684 nuclear (c) RNA isolated from left or right cortex of the same mice at 6 weeks of age (n=2). **(d)**
685 *Top*, Diagram of RNA distribution across subcellular compartments. *Bottom,* Area proportional
686 Venn diagram comparing overlap in gene expression changes between nuclear RNA, whole cell
687 RNA, and nascent RNA. **(e)** Cumulative distribution function of gene lengths for all upregulated
688 and downregulated protein-coding genes among nascent, nuclear, and whole cell RNA pools (n =
689 10,390 genes, Kolmogorov-Smirnov). **(f)** *Top,* Boxplots depicting median $\log_2$ fold changes in
690 R106W mice between nascent, nuclear, and whole cell RNA pools, classified by the direction of
691 gene misregulation (n = 10, 390 genes, Pairwise Wilcoxon Rank Sum *P* displayed). Gene groups
692 are arranged by median gene length (black bar on top). Arrows highlight the percentage of
693 10,390 genes that display similar (38.4% of expressed genes), opposite (48%), or dynamic
694 changes (13.6%) across subcellular RNA pools. *Bottom,* Heatmap displaying statistical
695 enrichment of T158M and R106W DEGs in excitatory neurons among gene groups (One-tailed
696 Fisher's Exact Test). **(g)** DAVID Gene ontology terms (Benjamini $P < 0.01$, FDR < 0.05) for
697 Group A and Group G sets of genes defined in (f). **(h)** *Top*, Diagram of RT-PCR primer design
698 to measure mature and primary RNA transcripts. *Bottom*, Data shows overall trend in gene

699 expression mean fold changes using primers against primary and mature RNA transcripts (*left*)
700 or primary transcripts only (*right*)_across individual genes from Group A/C (n = 7 genes), Group
701 B (n = 5 genes), and Group D (n = 5 genes) in R106W compared to TAVI mice (Two-way
702 ANOVA). Data depicts mean ± S.D. **(i)** Mean $\log_2$ fold change in 6-week R106W (red; n = 4)
703 and T158M (orange, n = 4) sorted excitatory (*left*) and inhibitory neurons (*right*) using genes that
704 are also detected in GRO-seq. **P* < 0.5, ***P* < 0.01, ****P* < 0.001, *****P* < 0.0001, n.s. = not
705 significant. See also **Supplementary Figs. 7-9**.

Figure 5. T158M and R106W differentially expressed genes in mosaic female mice. **(a)** RTT-like phenotypic score in TAVI (n = 12), T158M (n = 4), and R106W (n = 9) heterozygous female mice (Two-way ANOVA). Data depicts mean ± SEM. **(b)** FACS isolation of excitatory neuronal nuclei from the cortex of heterozygous TAVI, T158M, or R106W female mice. **(c)** Biotin signal intensity from FACS-isolated populations depicted in (b) (n_{T158M} = 4, n_{R106W} = 9, Two-way ANOVA). Data depicts mean ± SEM. **(d)** X-inactivation ratios among cortical excitatory neurons in all sorted female mice, displayed as a percentage of the FACS-sorted WT population (n_{TAVI} = 12, n_{T158M} = 4, n_{R106W} = 9, One-way ANOVA). Data points in red indicate samples used for RNA-seq. Data depicts mean ± SEM. **(e)** Bar graph showing the cell and non-cell autonomous distribution of total protein-coding DEGs identified from T158M and R106W female mice. **(f)** Principal component analysis of WT and MUT cell populations isolated from TAVI, T158M, and R106W female mice. **(g)** Heatmap displaying $\log_2$ fold changes among the total number of protein-coding DEGs detected in both WT and MUT populations from T158M or R106W female mice. Note genes that overlap across genotype (n = 194). **(h)** Proportion of cell autonomous (CA) and non-cell autonomous (NCA) genes that overlap between T158M and R106W female excitatory neurons (One-tailed Fisher's Exact Test). **(i)** Boxplots comparing absolute $\log_2$ fold change between cell autonomous and non-cell autonomous shared DEGs (n = 185) between T158M and R106W female mice (One-tailed Wilcoxon Signed Rank). **(j)** Enrichment map of pre-ranked GSEA functional network associations (*P-value* < 0.01, *Q-value* < 0.1). Data represents DEGs that overlap between T158M and R106W mice (n = 185). Nodes denote functional categories, colored by Normalized Enrichment Score (NES). Line weight denotes extent of gene overlap between connected nodes. **P* < 0.5, ***P* < 0.01, ****P* < 0.001, *****P* < 0.0001, n.s. = not significant. See also **Supplementary Fig. 10**.

	Experiment	Cell Type	Genotype	Differentially Expressed Genes (DEGs)			Upregulated/ Downregulated (Protein-coding)	$\lvert Log_2$ Fold Change$\rvert$ (Protein-coding)	Gene Length (kb) (Protein-coding)	Proportion of Cell Type Enriched Genes (Protein-coding)		
				Total	Coding	Non-coding		Median [IQR]	Median [IQR]	Constitutive	Excitatory (EXC)	Inhibitory (INH)
6 WEEK Males	Actively Expressed Genes	Excitatory Neurons	TAVI (Control)	13877	10926	2951	-	-	24.9 [9.9 - 61.3]	46.5%	28.5%	24.9%
		Inhibitory Neurons	TAVI (Control)	10369	8319	2050	-	-	25.4 [10.3 - 61.5]	46.8%	24.3%	28.8%
	Cell Type-enriched Gene Expression	Excitatory Neurons	TAVI (Control)	4593	3958	635	-	0.75 [0.41 - 1.46]	50.6 [21.5 - 110.1]	-	100%	-
		Inhibitory Neurons	TAVI (Control)	4783	4194	589	-	0.73 [0.45 - 1.47]	21.2 [8.8 - 53.0]	-	-	100%
	MeCP2-dependent Gene Expression	Excitatory Neurons	T158M	197	177	20	63.8% DOWN	0.45 [0.33 - 0.62]	88.6 [33.5 - 173.1]	16.4%	49.2%	34.5%
			R106W	425	386	39	61.7% DOWN	0.44 [0.34 - 0.61]	82.5 [36.7 - 146.0]	17.6%	51.3%	31.1%
			Shared DEGs	75	69	6	65.2% DOWN	see Figure 3D	109.8 [49.9 - 184.1]	14.5%	52.2%	33.3%
		Inhibitory Neurons	T158M	146	143	3	62.9% UP	0.45 [0.29 - 0.55]	107.8 [41.4 - 188.7]	20.3%	44.8%	35.0%
			R106W	758	697	61	56.2% UP	0.41 [0.33 - 0.56]	40.5 [19.1 - 102.9]	29.4%	35.3%	35.3%
			Shared DEGs	109	107	2	64.5% UP	see Figure 3D	112.8 [42.9 - 202.8]	18.7%	46.7%	34.6%
18 WEEK Females	MeCP2-dependent Gene Expression	Excitatory Neurons	$T158M_{WT}$	42	28	14	64.3% DOWN	0.52 [0.49 - 0.79]	54.6 [27.2 - 112.6]	-	-	-
			$R106W_{WT}$	346	294	52	62.2% UP	0.64 [0.47 - 0.93]	51.4 [21.0 - 140.4]	-	-	-
			$T158M_{MUT}$	585	516	69	67.2% DOWN	0.49 [0.40 - 0.73]	51.2[20.4 - 113.2]	-	-	-
			$R106W_{MUT}$	634	569	65	52.2% UP	0.54 [0.43 - 0.83]	65 [31.7 - 142.1]	-	-	-
			$Shared_{MUT}$	207	185	22	65.9% DOWN	see Figure 5I	77.5 [36.2 - 143.6]	-	-	-

Table 1 Summary of Differentially Expressed Genes (DEGs) identified in the study

Online Methods

Generation of Mouse Lines The targeting construct used for homologous recombination at the *Mecp2* locus in murine ES cells was cloned in two arms by PCR amplification of sv129 genomic DNA. The 5′ arm was PCR amplified with 5′ -AGGAGGTAGGTGGCATCCTT-3′ and 5′ -CGTTTGATCACCATGACCTG-3′ primers, whereas the 3′ arm was PCR amplified with 5′ -GAAATGGCTTCCCAAAAAGG-3′ and 5′ -AAAACGGCACCCAAAGTG-3′ primers. Restriction sites at the ends of each arm were created using nested primers for cloning into a vector containing a *loxP*-flanked neomycin cassette (Neo) and a diphtheria toxin A negative-selection cassette. QuikChange (Stratagene) insertional mutagenesis was used to generate the *Mecp2*^{Tavi} targeting construct by inserting the Tavi tag immediately upstream of the *Mecp2* stop codon within the 5' arm. The portion of the Tavi tag containing the biotinylation consensus sequenced flanked by 5' NaeI and 3' BspHI restriction sites was inserted through two rounds of mutagenesis:

Round 1 Forward: 5'-
GACCGAGAGAGTTAGCGCCGGCCTGAACGACATCTTCGAGTCATGACTTTACATAG
AGCG-3'

Round 1 Reverse: 5'-
CGCTCTATGTAAAGTCATGACTCGAAGATGTCGTTCAGGCCGGCGCTAACTCTCTCG
GTC-3'

753 Round 2 Forward: 5'-

754 CTGAACGACATCTTCGAGGCTCAGAAAATCGAATGGCACGAATCATGACTTTACATA

755 GAG-3'

756 Round 2 Reverse: 5'-

757 CTCTATGTAAAGTCATGATTCGTGCCATTCGATTTTCTGAGCCTCGAAGATGTCGTTC

758 AG-3'

759

760 The portion of the tag containing the TEV protease cleavage site was inserted upstream of the

761 NaeI restriction site with a third round of mutagenesis:

762

763 Round 3 Forward: 5'-

764 GACCGAGAGAGTTAGCGAAAACCTGTATTTTCAGGGCGCCGGCCTGAACGACATC-3'

765 Round 3 Reverse: 5'-

766 GATGTCGTTCAGGCCGGCGCCCTGAAAATACAGGTTTTCGCTAACTCTCTCGGTC-3'

767

768 To generate *Mecp2*^{Tavi} targeting constructs bearing independent RTT-associated point

769 mutations, QuikChange site-directed mutagenesis was used to mutate MeCP2 arginine 106 to

770 tryptophan and MeCP2 threonine 158 to methionine within the 3'arm and 5'arm, respectively. A

771 single nucleotide at codon T160 also underwent site-directed mutagenesis for a silent mutation to

772 introduce a BstEII restriction site to correctly identify targeted ES cells.

773 To generate conditional *R26*^{cBirA} transgenic mice, PCR primers containing AscI

774 restriction sites and a Kozak consensus sequence were used to subclone the *BirA* coding

775 sequence and insert it downstream of both a CAG promoter and a floxed transcriptional

attenuator, *Neo-STOP*, within pROSA26-1, a transgenic targeting vector that has previously been characterized[56].

After confirmation by Sanger sequencing and linearization with NotI (*Mecp2*^{Tavi} targeting construct and its mutant variants) or SgfI (*cBirA* targeting construct), the constructs were electroporated into sv129-derived murine ES cells. Correctly targeted ES cells were independently injected into C57BL/6 blastocysts and subsequently implanted into pseudopregnant females. Agouti offspring were screened by southern blot and PCR genotyping to confirm germline transmission of the *Mecp2*^{Tavi}, *Mecp2*$^{T158M\text{-}Tavi}$, *Mecp2*$^{R106W\text{-}Tavi}$, and *R26*^{cBirA} alleles. In the case of the *Mecp2*^{Tavi} allele and its mutant variants, the resulting offspring were mated with C57BL/6 *EIIa-cre* mice to ensure germline deletion of the floxed Neo cassette between *Mecp2* exons 3 and 4.

Additional Mouse lines *Dlx5/6-Cre* (Stock #008199) and *EIIa-Cre* (Stock #003724) mice were obtained from The Jackson Laboratory (Bar Harbor, ME)[31,36]. *NeuroD6/NEX-Cre* mice were obtained with permission from the Nave Laboratory[35].

Animal Husbandry Experiments were conducted in accordance with the ethical guidelines of the US National Institutes of Health and with the approval of the Institutional Animal Care and Use Committee of the University of Pennsylvania. All of the experiments described were performed using mice on a congenic sv129:C57BL/6J background with the knock-in/transgenic alleles backcrossed to C57BL/6J mice (The Jackson Laboratory) for at least five generations, unless otherwise stated. Mice were housed in a standard 12h light/12h dark cycle with access to ample amounts of food and water. Mice bearing the Tavi tag were genotyped using a bipartite

primer PCR-based strategy to detect the Tavi tag at the 3'-end of the endogenous *Mecp2* gene (Forward: 5'-CACCCCGAAGCCACGAAACTC-3', Reverse: 5'-TAAGACTCAGCCTATGGTCGCC-3') and give rise to a 318-bp product from the wild-type allele and a 388-bp product from the tagged allele. Mice bearing the *BirA* transgene were genotyped using a tripartite primer PCR-based strategy to detect the presence or absence of the CAG promoter at the *Rosa26* locus (Forward:5'-TGCTGCCTCCTGGCTTCTGAG-3', Reverse #1: 5'-GGCGTACTTGGCATATGATACAC-3', Reverse #2: 5'-CACCTGTTCAATTCCCCTGCAG-3') and give rise to a 173-bp product from the wild-type allele and a 477-bp product from the transgene-bearing allele. Mice bearing Cre-recombinase (either *NeuroD6/NEX-Cre* or *Dlx5/6-Cre*) were genotyped using PCR-based strategies as previously described[35,36].

Phenotypic Assessment For tagged *Mecp2* knock-in mice, phenotypic scoring was performed on a weekly basis for the presence or absence of overt RTT-like symptoms as previously described[33]. Investigator was blinded to genotypes during phenotypic assessment of mice. For BirA transgenic mice, no formal scoring was performed. However, $R26^{BirA}$ heterozygous and homozygous mice are viable, fertile, and devoid of any gross abnormalities, consistent with previously engineered transgenic mice that express BirA either ubiquitously or within restricted tissues using cell type-specific promoters[57,58].

Immunofluorescence and Microscopy Mice were anesthetized with 1.25% Avertin (wt/vol), transcardially perfused with 4% paraformaldehyde (wt/vol) in 0.1M sodium-potassium phosphate buffered saline and postfixed overnight at 4°C. Brains were coronally or sagittally

822 sectioned at 20µm using a Leica CM3050 S cryostat. Immunofluorescence on free-floating
823 sections was performed as previously described[18], except sections were permeabilized with 0.5%
824 Triton without methanol for 20 minutes, and sections were blocked overnight with 10% Normal
825 Goat Serum and 1:100 unconjugated goat anti-mouse IgG (Sigma M5899). The following
826 primary antibodies were incubated at 4°C overnight: rabbit anti-MeCP2 C-terminus (1:1000, in
827 house), rabbit anti-nucleolin (1:1000, Abcam ab22758), mouse anti-parvalbumin (1:500,
828 Millipore MAB1572), rabbit anti-calretinin (1:1000, Swant 7699/3H), mouse anti-GAD67
829 (1:500, Millipore MAB5406), mouse anti-NeuN (1:500, Millipore MAB377). For rat anti-
830 somatostatin (1:250, Millipore MAB354MI), primary incubation was performed for 48 hours at
831 4°C. Fluorescence detection of primary antibodies was performed using Alexa 488-conjugated
832 goat anti-rabbit (1:1000, Invitrogen A11008), Alexa 488-conjugated goat anti-mouse (1:1000,
833 Invitrogen A11029), or Alexa 488 goat anti-rat (1:1000, Invitrogen A11006). Fluorescence
834 detection of biotin was performed simultaneously with Streptavidin Dylight 650 (1:1000, Fisher
835 84547) for fluorescence microscopy and Streptavidin Dylight 550 (1:1000, Fisher 84542) for
836 confocal microscopy. Sections were counterstained with DAPI (1:1000, Affymetrix 14564) to
837 visualize DNA before mounting with Fluoromount G (SouthernBiotech). Images were acquired
838 using a Leica DM5500B fluorescent microscope with a Leica DFC360 FX digital camera
839 (region-specific biotinylation, quantification of neuronal cell type-specific markers) or a Leica
840 TCS SP8 Multiphoton confocal microscope (representative images of neuronal cell type specific
841 markers, subcellular localization of MeCP2). Images were acquired using identical settings for
842 laser power, detector gain amplifier offset and pinhole diameter in each channel. Image
843 processing was performed using ImageJ and Adobe Photoshop, including identical adjustments

of brightness, contrast, and levels in individual color channels and merged images across genotypes.

Quantitative Western analysis Quantitative Western blot was performed using Odyssey Infrared Imaging System (Licor). Primary antibodies used in this study include rabbit anti-MeCP2 C-terminus (1:4000, in house), mouse anti-MeCP2 N-terminus (1:4000, Sigma M7433), mouse anti-NeuN (1:500, Millipore MAB377), rabbit anti-Avi tag (1:5000, Abcam ab106159, listed as anti-Tavi in main text, detects the minimal peptide substrate of biotin ligase BirA regardless of biotinylation status), rabbit anti-HDAC3 (1:1000, Santa Cruz sc-11417), rabbit anti-TBLR1 (1:1000, Bethyl A300-408A), rabbit anti-Sin3A, (1:500, Thermo Scientific PA1-870), rabbit anti-Histone H3 (1:1000, Abcam ab1791), and rabbit anti-TBP (1:1000, Cell Signaling #8515). Secondary antibodies include anti-rabbit IRDye 680LT (1:10,000, Licor), anti-mouse IRDye 800CW (Licor), Streptavidin Dylight 650 (1:10,000, Fisher 84547) and Streptavidin Dylight 800 (1:10,000, Fisher 21851). Quantification of protein expression levels was carried out following Odyssey Infrared Imaging System protocols. Scans of full-length Western blot membranes are provided in Supplementary Figs. 11-13.

Co-immunoprecipitation using nuclear extracts Tissues were mined on ice and homogenized in ice cold lysis buffer (10 mM HEPES pH 7.9, 1.5mM $MgCl_2$, 10mM KCl, 0.5% NP-40, 0.2mM EDTA, protease inhibitors). Nuclei were pelleted, washed and resuspended in nuclear extract (NE) buffer (20mM HEPES pH 7.9, 1.5mM $MgCl_2$, 500mM KCl, 0.2mM EDTA, 10% glycerol, protease inhibitors). Nuclei were incubated in NE buffer at 4°C for two hours with rotation. Samples were cleared by ultracentrifugation with a TLA 100.3 rotor (Beckman Optima TL) at

867 4°C for 30 minutes and the supernatant taken for nuclear extract. Protein concentration was
868 quantified using a modified Bradford assay (Bio-Rad). 1mg of nuclear extract was adjusted to
869 300µl total volume with NE buffer to perform IP in duplicate. Protein G Dynabeads or
870 Streptavidin M-280 Dynabeads (Life Technologies) were washed three times in PBS with 0.1%
871 Tween-20 and 0.1% BSA. Nuclear extracts were cleared for 30 minutes at 4°C with 25µl Protein
872 G Dynabeads. For streptavidin pulldown, 50µl of Streptavidin M-280 Dynabeads were added to
873 the nuclear extract and incubated at 4°C for two hours with rotation. To test if the Tavi tag was
874 required for streptavidin pulldown, nuclear extracts were split and incubated with or without
875 200U TEV protease (Invitrogen) in the absence of a reducing agent and without agitation at 4°C
876 for ≥ 4 hours prior to IP. For antibody immunoprecipitations, 5µg of antibody was added to the
877 nuclear extract and incubated overnight at 4°C with rotation. Protein G beads were blocked in
878 wash buffer overnight at 4°C with rotation. Blocked beads were then incubated with antibody-
879 bound nuclear extract for two hours at 4°C with rotation. Beads were washed four times in PBS
880 with 0.1% Tween-20 and split into two equal volumes. Each sample was resuspended in 25µl
881 loading buffer with 50mM DTT and boiled for 10 minutes at 95°C prior to loading on a 4-12%
882 Bis-Tris NuPage gel (Life Technologies).
883
884 **Chromatin immunoprecipitation** Forebrain tissues from male mice at 20 weeks of age were
885 homogenized in cross-linking buffer (1% formaldehyde (wt/vol), 10mM HEPES (pH 7.5),
886 100mM NaCl, 1mM EDTA, 1mM EGTA) and cross-linked for 5 minutes at RT. After quenching
887 with 125mM glycine, cross-linked tissue was washed with ice-cold PBS and dounced with 16
888 strokes in lysis buffer (50mM HEPES (pH 7.5), 140mM NaCl, 1mM EDTA, 1mM EGTA, 10%
889 glycerol (vol/vol), 0.5% NP-40 (vol/vol), and 0.25% Triton X-100 (vol/vol) with protease

890 inhibitors). Nuclei were pelleted, washed and resuspended in chromatin buffer (10mM Tris-HCl
891 (pH 8.0), 1mM EDTA, and 0.5mM EGTA with protease inhibitors). Chromatin was sonicated
892 using a Diagenode Bioruptor, and salt and detergent were added to adjust the chromatin buffer to
893 0.5% Triton X-100, 150mM NaCl, 10mM EDTA, and 0.1% sodium deoxycholate (DOC,
894 vol/vol), and precleared at 4°C with Protein A Dynabeads (Invitrogen). For
895 immunoprecipitation, 3µg of purified rabbit anti-MeCP2 IgG (in house) or non-specific rabbit
896 IgG control (Millipore NI01) was incubated with 45µg of chromatin for 4 hours, followed by an
897 overnight incubation with pre-blocked Protein A Dynabeads, at 4°C with rotation. Bead-bound
898 chromatin was washed with low salt buffer (50mM HEPES pH 7.5, 150mM NaCl, 1mM EDTA,
899 1% Triton X-100, 0.1% DOC), high salt buffer (50mM HEPES pH 7.5, 500mM NaCl, 1mM
900 EDTA, 1% Triton X-100, 0.1% DOC), LiCl buffer (50mM Tris-HCl pH 8.0, 150mM NaCl,
901 1mM EDTA, 0.5% NP-40, 0.5% DOC) and TE buffer (10mM Tris-HCl pH 8.0, 1mM EDTA).
902 Chromatin was eluted with elution buffer (50mM Tris-HCl pH 8.0, 10mM EDTA, and 1% SDS
903 (wt/vol)), digested with proteinase K (0.5mg ml^{-1}), and reversed crosslinked at 65°C overnight.
904 After RNase A treatment, DNA fragments were extracted with phenol/chloroform and ethanol-
905 precipitated.
906 Quantitative real-time PCR (qPCR) analysis was carried out using SYBR green detection
907 (Life Technologies) on an ABI Prism 7900HT Real-Time PCR System (Applied Biosystems).
908 The percent input for each amplicon was determined by comparing the average threshold cycle
909 of the immunoprecipitated DNA to a standard curve generated using serial dilutions of the input
910 DNA and interpolating the “fraction of input” value for this sample.
911

Sub-nuclear Fractionation To prepare nucleoplasm-enriched proteins, cortices were dounce homogenized in 5 ml NE10 buffer (20 mM HEPES, pH 7.5, 10 mM KCl, 1 mM $MgCl_2$, 0.1% Triton X-100, and 15 mM β-mercaptoethanol) 30 times using a loose pestle. The resulting nuclei were washed with NE10 buffer and rotated in NE300 buffer (20 mM HEPES, pH 7.5, 300 mM NaCl, 10 mM KCl, 1 mM $MgCl_2$, 0.1% Triton X-100, and 15 mM β-mercaptoethanol) for 1 hour at 4°C. Samples were centrifuged at 500 *g* for 5 minutes, and the supernatant, which represents the nucleosolic fraction, was collected and saved. The insoluble pellet, consisting of the chromatin-bound fraction, was washed in NE150 buffer and incubated with 500 units of benzonase (Sigma-Aldrich) for 5 minutes at room temperature. The pellet was then resuspended in 50 µl NE150 buffer (20 mM HEPES, pH 7.5, 150 mM NaCl, 10 mM KCl, 1 mM $MgCl_2$, 0.1% Triton X-100, and 15 mM β-mercaptoethanol) and rotated for 1 hour at 4°C. Samples were centrifuged at 16,000 *g*, and the supernatant was collected as the chromatin-bound fraction.

FACS Isolation of Neuronal Nuclei for RT-PCR and RNA-seq Nuclei were isolated from fresh cortical tissue for FACS under ice-cold and nuclease-free conditions. Mouse cortices were rapidly resected on ice and subjected to dounce homogenization in homogenization buffer (0.32M sucrose, 5mM $CaCl_2$, 3mM $MgAc_2$, 10mM Tris-HCl pH 8.0, 0.1% Triton, 0.1mM EDTA, Roche Complete Protease Inhibitor without EDTA). Homogenates were layered onto a sucrose cushion (1.8M sucrose, 10mM Tris-HCl pH 8.0, 3mM $MgAc_2$ Roche Complete Protease Inhibitor without EDTA) and centrifuged in a Beckman Coulter L7 Ultracentrifuge at 25,000 rpm at 4°C for 2.5 hours using a Beckman Coulter SW28 swinging bucket rotor. Nuclei were resuspended & washed once in blocking buffer (1x PBS, 0.5% BSA (Sigma A4503), RNasin Plus RNase Inhibitor (Promega)) and pelleted using a tabletop centrifuge at 5000 RCF at 4°C for

10 minutes. Nuclei were resuspended in blocking buffer to a concentration of ~6x10^6 nuclei/ml, blocked for 20 minutes at 4°C with rotation, then incubated with Streptavidin Dylight 650 (1:1000, Fisher 84547) and Alexa 488-conjugated anti-NeuN antibody (1:1000, Millipore MAB377X) for 30 minutes at 4°C with rotation. After a 5-minute incubation with 1:1000 DAPI to enable singlet detection during FACS, labeled nuclei were washed for an additional 30 minutes at 4°C with blocking buffer, pelleted and resuspended in blocking buffer with 1% BSA. A BD Biosciences Influx cell sorter at the University of Pennsylvania Flow Cytometry and Cell Sorting Facility was used to identify cell type-specific populations of nuclei, and 1.2 – 2.5 x10^5 singlet nuclei from specified populations were directly sorted into Qiagen Buffer RLT Plus for immediate lysis and stabilization of RNA transcripts. Total nuclear RNA was processed using the Qiagen AllPrep DNA/RNA mini kit according to manufacturer instructions, with exception to the on-column DNaseI treatment. RNA was eluted from RNeasy mini spin columns and treated with DNaseI (Qiagen 79254) for 25 minutes at room temperature, then precipitated with glycogen/NaOAc and stored in ethanol at -80°C. Ethanol precipitation of nuclear RNA was carried out to completion prior to initiating RT-PCR or RNA-seq library construction.

For RNA-seq, total RNA was prepared from FACS-isolated cortical nuclei of male mice at 6 weeks (TAVI, T158M, R106W, 2-3 mice pooled per biological replicate, 4 independently-sorted biological replicates total) and female mice at 18 weeks (TAVI, T158M, R106W, 1 single mouse per biological replicate, 2 independently-sorted biological replicates total). No method of randomization was used to determine how animals were allocated to experimental groups, which was determined by genotype with matching age and sex. The numbers of biological replicates used for differential gene expression analysis are in compliance with ENCODE consortium long RNA-seq recommendations (≥2 replicates). Furthermore, the total amount of RNA isolated from

120,000-250,000 sorted nuclei was used as input for library construction; hence differential gene expression comparisons between FACS-isolated *Mecp2* control and mutant neurons are performed using RNA from equivalent numbers of neuronal nuclei. Total RNA was depleted of ribosomal RNAs, subjected to 5 minutes of heat fragmentation, and converted to strand-specific cDNA libraries using the TruSeq Total RNA library prep kit with RiboZero depletion (Illumina). Multiplexed libraries were submitted for 100 paired-end sequencing on the Illumina HiSeq 2000/2500 platform at the University of Pennsylvania Next Generation Sequencing Core facility, yielding approximately 30-40M total reads per library. 90-95% of total reads were uniquely mapped to the mouse Ensembl GRCm38/mm10 mouse genomic assembly.

Real-Time PCR (RT-PCR) For RT-PCR of FACS-isolated cortical nuclei, total RNA was prepared (as described in preceding section) from 120,000 sorted nuclei of TAVI or R106W male mice at 6 weeks of age (2-3 mice pooled per biological replicate, 3 independently-sorted biological replicates total). For remaining RT-PCR assays, total RNA was isolated from whole tissue or unsorted cortical nuclei of WT, TAVI, T158M, or R106W mice as specified in figure legends (1 mouse per biological replicate, 3 biological replicates total). Total RNA was converted to cDNA with random hexamers using the SuperScript III First-Strand Synthesis System (Invitrogen). RT-PCR was performed on a ABI Prism 7900HT Real-Time PCR System (Applied Biosystems). To validate cell type-specific cortical nuclei populations (Fig. 2d and Supplementary Fig. 3i-j), exon-spanning Taqman gene expression assays to detect mRNA transcripts for the following genes: *CRE* (Mr00635245_cn), *Mecp2* (Mm01193537_g1), *Rbfox3* (Mm01248771_m1), *Gfap* (Mm01253033_m1), *Aif1* (Mm00479862_g1), *Mog* (Mm00447824_m1), *Slc17a7* (Mm00812886_m1), *Tbr1* (Mm00493433_m1), *Gad1*

(Mm04207432_g1), *Slc35a1* (Mm00494138_m1), *Ht3ar* (Mm00442874_m1), *Pvalb* (Mm00443100_m1), *Sst* (Mm00436671_m1), *Pgk1* (Mm00435617_m1), *Actb* (Mm00607939_s1), *ß2m* (Mm00437762_m1). A geometric mean was calculated to normalize mRNA expression levels to multiple housekeeping genes (*Actb*, *ß2m*, and *Pgk1*), and cell type-enrichment for each sorted population was determined relative to the total mixed population of DAPI+ nuclei. For RT-PCR validation of low expressing genes and subcellular gene expression changes (Fig. 4h and Supplementary Figure 8), primers against primary transcripts and mRNAs were used (listed in Supplementary Table 2), and geometric means were calculated to normalize mRNA expression levels to multiple housekeeping genes (*Actb*, *ß2m*, and *Pgk1*).

GRO-seq Nuclei were isolated from fresh cortical tissue of TAVI or R106W male mice at 6 weeks of age (2 mice pooled per biological replicate, 2 biological replicates total) under ice-cold and nuclease-free conditions as described in the preceding section. After ultracentrifugation, nuclei were resuspended & washed once in PBS (1x PBS, RNasin Plus RNase Inhibitor (Promega)) and pelleted using a tabletop centrifuge at 5000 RCF at 4°C for 10 minutes. Nuclei were resuspended in PBS, pipetted through a 0.22µm filter and counted using a hemocytometer. Nuclei were then pelleted, resuspended to a concentration of 5×10^6 - 10×10^6 nuclei/100µl in glycerol storage buffer (50mM Tris pH 8.3, 40% glycerol, 5mM $MgCl_2$, 0.1 mM), and flash frozen in liquid N_2 for storage until needed.

For each nuclear run-on (NRO), 100µl of nuclei was mixed with 46.5µl NRO Reaction Buffer (10mM Tris pH 8.0, 5mM $MgCl_2$, 1 mM DTT, 300mM KCl), 3.5µl Nucleoside Mix (50µM ATP, 50µM GTP, 2µM CTP, 50µM Br-UTP, 0.4U/µl RNasin), and 50µl 2% Sarkosyl

Nuclear Run On Stop Solution (20mM Tris pH 7.4, 10mM EDTA, 2% SDS). The NRO reaction was performed at 30°C for 5 minutes, then terminated by a 20 minute incubation with DNAse I at 37°C, followed by a hour-long incubation with 225µl NRO Stop Buffer (20mM Tris, pH 7.4, 10mM EDTA, 2% SDS) and Proteinase K at 55°C. Phenol-extracted RNA was fragmented with 0.2N NaOH, and BrdU-RNA was isolated three consecutive times with BrdU-antibody beads, treated with enzymatic tobacco acid pyrophosphatase (TAP) and T4 polynucleotide kinase (PNK) to remove the cap and 3'-phosphate and to add a 5'-phosphate, as well as Illumina TruSeq small RNA sample prep kit adapter ligations between BrU-RNA isolation steps as described[41,59].

RNA-seq Mapping, Read Counting, and Differential Expression Analysis The mouse mm10 genomic sequence (Mus_musculus.GRCm38.75.dna.primary_assembly.fa.gz) and gene information (Mus_musculus.GRCm38.75.gtf.gz) were downloaded from Ensembl release 75. The genome files used for mapping were built by STAR (version 2.3.0)[60] using the parameters '*STAR --runMode genomeGenerate --runThreadN 12 --genomeDir ./ --genomeFastaFiles Mus_musculus.GRCm38.75.dna.primary_assembly.fa.gz --sjdbGTFfile Mus_musculus.GRCm38.75.gtf --sjdbOverhang 100*'. The FASTQ files were mapped to the mouse Ensembl GRCm38/mm10 genome assembly by STAR (version 2.3.0) using the parameters *'--genomeDir ENSEMBL_75_mm10 --runThreadN 10 --outFilterMultimapNmax 1 --outFilterMismatchNmax 3*'. Perl scripts generated in-house were used to count the number of read pairs that mapped to genic regions (exon + intron) for each gene. If one end of a read pair overlapped with the annotated genomic region of a given gene and the other did not, the read pair was included in the final count for that gene. The total number of

read pairs that overlapped within a given gene represented the final read count for that gene. All intron and exon-mapped reads were used for differentially expressed gene comparisons, which were performed by using the R packages "edgeR" (v3.10.0)[61] and "DEseq2" (v1.8.0)[62]. Genes exhibiting low expression due to a substantially low number of mapped reads and whose edgeR CPM values satisfied the condition '*rowSums(cpm(data_y)) < 2*' were filtered out from differential gene expression analyses. Conversely, genes with '*rowSums(cpm(data_y)) ≥ 2*' were retained for differential gene expression analyses. A false discovery rate < 0.05 was set to identify differentially expressed genes, and no fold change cutoff was applied. For each comparison, the results of both edgeR and DESeq2 analyses were merged into a final non-redundant and FDR-controlled list of genes to avoid method-specific biases. The mean fold change and the mean FDR generated from both methods were used for generating plots and heatmaps.

RNA Binding Protein (RBP) Data Pre-processing and Analysis To determine the enrichment of neuronally expressed RNA-binding proteins on gene transcripts, raw HITS-CLIP reads derived from the mouse brain were obtained from publically available datasets in the GEO repository (listed below). The quality of raw reads were assessed with FastQC[63] and contaminants were removed using Trimgalore[64] with parameters *'-q 15 --length 20 --stringency 5*'. Remaining reads were aligned to a mouse reference genome derived from the Ensembl v75 archived assembly using STAR (version 2.5)[60] with parameters '*--outFilterMultimapNmax 1 --outFilterScoreMinOverLread 0 --outFilterMatchNminOverLread 0.5 --alignEndsType Local*'. Replicates were merged and then subsampled to match the sample with the lowest library size. Genome annotation from Ensembl v75 and in-house developed scripts facilitated the calculation

of RNA binding protein coverage in gene models. Genes not included in Groups A-H (Figure 4f) were filtered out. For k-means clustering of RBPs, raw read counts were first normalized using the variance stabilizing transformation function in "DESeq2"[62], and the R packages "factoextra", "cluster", and "NbClust" were used to perform a Silhouette coefficient analysis and cluster genes based on the optimal k number of clusters. The Kruskal-Wallis test, followed by a post-hoc Wilcoxon Rank Sum Test with Holm's correction for multiple comparisons, was used to identify statistically significant differences in RNA-binding protein enrichment within each gene cluster. RBP gene clusters were then used to perform One-tailed Fisher's Exact Test with genes from Groups A-H to identify RBP enrichments that significantly associate with genes displaying subcellular differences in gene expression changes in R106W mutant mice.

HITS-CLIP datasets used for RBP Analysis		
AGO2 (Rep 1-6/9-12)	GSE73058	PMID: 26602609
APC (Rep 1-4)	SRP042131	PMID: 25036633
MBNL1 (Rep 1-2)	GSE39911	PMID: 22901804
MBNL2 (Rep 1-3)	GSE38497	PMID: 22884328
ELAVL1 (Rep 1-2)	GSE45148	PMID: 21784246
FMR1 (Rep 1-2)	GSE45148	PMID: 21784246
FUS (Rep 1-3)	GSE40651	PMID: 23023293
TAF15 (Rep 1-2)	GSE43294	PMID: 23416048
TDP43	GSE40651	PMID: 23023293
RBFOX1	SRP030031	PMID: 24213538
RBFOX2	SRP030031	PMID: 24213538
RBFOX3 (Rep 1-5)	SRP039559	-

Functional Enrichment of Differentially Expressed Genes For DAVID gene ontology, a list of differentially expressed protein-coding genes was compared to a background list of actively expressed protein-coding genes from their respective cell type. Statistically significant terms (Benjamini $P < 0.01$, FDR < 0.05) were plotted for Figures S3C-D. For Gene Set Enrichment Analysis (GSEA), we performed a seeded, pre-ranked GSEA from lists of differentially

1066 expressed protein-coding genes (ranked by fold change) using the September 2015 Mouse GO
1067 Gene Set Release (http://download.baderlab.org/EM_Genesets/September_24_2015/Mouse/).
1068 GSEA network associations (*P-value* < 0.1, *Q-value* < 0.1) were visualized using the Enrichment
1069 Map application (v2.0.1) in Cytoscape (v3.2.1)[65,66], and clustered using gene set overlap
1070 coefficients.
1071
1072 **Principal Components Analysis (PCA)** PCA analyses were performed with the top 500 genes
1073 exhibiting the highest row variance using the "plotPCA" function in the R package "DESeq2".
1074 Principal components were plotted using Graphpad Prism version 6.0 for Mac (GraphPad
1075 Software, La Jolla California USA, www.graphpad.com).
1076
1077 **Determination of Actively Expressed Genes** Actively expressed genes for excitatory and
1078 inhibitory neurons were determined by calculating the normalized FPKM (zFPKM) and using
1079 ZFPKM ≥ 3 for the active gene cutoff as previously described[67].
1080
1081 **Statistical Analyses** Statistical analyses were performed using Graphpad Prism version 6.0 for
1082 Mac (GraphPad Software, La Jolla California USA, www.graphpad.com) and R[68]. No statistical
1083 method was used to estimate sample size, as pre-specified effect sizes were not assumed. No
1084 animals or samples were excluded from analyses. Individual statistical tests are fully stated in the
1085 main text or figure legends. Comparisons of normally distributed data consisting of two groups
1086 with equal variances (F-test equality of variance $P > 0.05$) were analyzed using Student's T-test,
1087 and unequal variances (F-test equality of variance $P < 0.05$) using Students T-test with Welch's
1088 correction for unequal variance. Comparisons of normally distributed data consisting of three or

more groups were analyzed using One-way ANOVA with the appropriate *post-hoc* test. Comparison of two or more factors across multiple groups was analyzed using a Two-way ANOVA with Sidak's correction for multiple comparisons. Comparisons of non-normally distributed data were analyzed using the Mann-Whitney/Wilcoxon test (two groups) or the Kruskal-Wallis test (three or more groups) with the appropriate *post-hoc* test. For multiple comparisons, all p-values are adjusted using the Holm-Bonferroni correction unless otherwise indicated. Experimental design and analytical details are also listed in the Life Sciences Reporting Summary.

Main Figure Statistical Analyses

Figure 1 Utilization and characterization of *Mecp2*^{Tavi} mice and associated RTT variants

(e) $n_{replicates} = 3$, One-way ANOVA [$F = 25.55$, $P = 0.0012$]; Tukey's multiple comparisons correction applied. **(f)** *Left*, $n_{WT} = 4$, $n_{TAVI} = 5$, $n_{T158M} = 4$, $n_{R106W} = 4$; One-way ANOVA [$F = 12.4$, $P = 0.0004$]; Sidak's multiple comparisons correction applied. *Right*, $n_{WT} = 4$, $n_{TAVI} = 5$, $n_{T158M} = 4$, $n_{R106W} = 4$;One-way ANOVA [$F = 0.2977$, $P = 0.8264$]; Sidak's multiple comparisons correction applied. **(g)** $n_{WT} = 20$, $n_{TAVI} = 11$, $n_{KO} = 6$, $n_{T158M} = 6$, $n_{R106W} = 12$; One-way ANOVA [$F = 20.05$, $P < 0.0001$]; Tukey's multiple comparison correction applied. **(j)** $n_{WT} = 31$, $n_{TAVI} = 23$, $n_{KO} = 17$, $n_{T158M} = 39$, $n_{R106W} = 26$, Mantel-Cox [$\chi^2 = 109.3$, df = 4, $P < 0.0001$].

Figure 2 Cell type-specific transcriptional profiling of neuronal nuclei

(d) $n_{replicates} = 3$, Two-way ANOVA, Control [Cell Type-Gene Interaction, $F = 42.68$, $P < 0.0001$; Cell Type, $F = 222.0$, $P < 0.0001$; Gene, $F = 80.03$, $P < 0.0001$], Non-Neuronal [Cell Type-Gene

Interaction, F = 12.47, $P < 0.0001$; Cell Type, F = 109.8, $P < 0.0001$; Gene, F = 7.655, $P = 0.0027$], EXC-specific [Cell Type-Gene Interaction, F = 4.376, $P = 0.0198$; Cell Type, F = 1227, $P < 0.0001$; Gene, F = 0.3267, $P = 0.5756$], INH-specific [Cell Type-Gene Interaction, F = 3.047, $P = 0.0040$; Cell Type, F = 646.5, $P < 0.001$; Gene, F = 2.916, $P = 0.033$]; Dunnett's multiple comparisons correction applied.

Figure 3 T158M and R106W differentially expressed genes at 6 weeks of age

(c) One-tailed Wilcoxon Signed Rank, Excitatory $P_{\text{Upregulated}} = 4.357\text{e-}3$, Excitatory $P_{\text{Downregulated}} = 7.345\text{e-}3$, Inhibitory $P_{\text{Upregulated}} = 4.575\text{e-}09$, Inhibitory $P_{\text{Downregulated}} = 1.684\text{e-}05$. **(e)** Chi-square Goodness-of-Fit, Excitatory $P_{\text{T158M}} < 2.2\text{e-}16$ [$\chi^2 = 182.2$, df = 2], Excitatory $P_{\text{R106W}} < 2.2\text{e-}16$ [$\chi^2 = 401.11$, df = 2], Inhibitory $P_{\text{T158M}} < 2.2\text{e-}16$ [$\chi^2 = 119.94$, df = 2], Inhibitory $P_{\text{R106W}} < 2.2\text{e-}16$ [$\chi^2 = 346.86$, df = 2]. **(f)** Two-tailed Kruskal-Wallis Rank Sum, Excitatory $P < 2.2\text{e-}16$ [$\chi^2 = 418.2$, df = 3], Inhibitory $P < 2.2\text{e-}16$ [$\chi^2 = 1026.9$, df = 3]; Pairwise Wilcoxon Rank Sum *P* displayed.

Figure 4 Genome-wide length-dependent transcriptional changes in RTT mutant mice

(e) *Top*, n = 10,390 genes, Kolmogorov-Smirnov $P < 2.2\text{e-}16$ for each nascent or nuclear RNA versus whole cell RNA comparison, no correction for multiple comparisons. **(f)** n = 10, 390 genes, Kruskal-Wallis $P_{\text{Group A}} < 2.2\text{e-}16$ [$\chi^2 = 2664.8$, df = 2], $P_{\text{Group B}} < 2.2\text{e-}16$ [$\chi^2 = 290.18$, df = 2], $P_{\text{Group C}} < 2.2\text{e-}16$ [$\chi^2 = 2403.3$, df = 2], $P_{\text{Group D}} < 2.2\text{e-}16$ [$\chi^2 = 319.36$, df = 2], $P_{\text{Group E}} < 2.2\text{e-}16$ [$\chi^2 = 1483.8$, df = 2], $P_{\text{Group F}} < 2.2\text{e-}16$ [$\chi^2 = 1385.8$, df = 2], $P_{\text{Group G}} < 2.2\text{e-}16$ [$\chi^2 = 2522.9$, df = 2], $P_{\text{Group H}} < 2.2\text{e-}16$ [$\chi^2 = 2442.7$, df = 2]; Pairwise Wilcoxon Rank Sum *P* displayed. **(h)** *Left*, Primary Transcripts + mRNA RT-PCR (Group Trend), $n_{\text{Group A/C}} = 7$ genes,

$n_{Group\ B}$ = 5 genes, $n_{Group\ D}$ = 5 genes, Two-way ANOVA, [Subcellular Compartment-Gene Group Interaction, F = 5.699, P = 0.0084; Subcellular Compartment, F = 1.419, P = 0.2436; Gene Group, F = 16.14, P < 0.0001]; Sidak's multiple comparisons correction applied. *Right*, Primary Transcripts only RT-PCR (Group Trend), $n_{Group\ A/c}$ = 7 genes, $n_{Group\ B}$ = 5 genes, $n_{Group\ D}$ = 5 genes, Two-way ANOVA, [Subcellular Compartment-Gene Group Interaction, F = 0.182, P = 0.8345; Subcellular Compartment, F = 0.1334, P = 0.7176; Gene Group, F = 15.12, P <0.0001]; Sidak's multiple comparisons correction applied.

Figure 5 T158M and R106W differentially expressed genes in mosaic female mice

(a) Two-way ANOVA [Genotype-Time Interaction, F = 2.987, P = 0.0712; Genotype, F = 41.14, P < 0.0001; Time, F = 7.332, P = 0.0129; Subjects (matching), F = 1.873, P = 0.0744]. **(b)** FACS isolation of cortical mosaic excitatory neuronal nuclei from heterozygous TAVI, T158M, or R106W female mice. **(c)** n_{T158M} = 4, n_{R106W} = 9, Two-way ANOVA [Population-Genotype Interaction, F = 0.3320, P = 0.5703; Population, F = 111.1, P < 0.0001; Genotype, F = 0.332, P = 0.5703]. **(d)** n_{TAVI} = 12, n_{T158M} = 4, n_{R106W} = 9, One-way ANOVA [F = 0.9376, P = 0.4067]. **(h)** One-tailed Fisher's Exact Test [Odds Ratio = 19.3, P = 2.43e-05]. **(i)** One-tailed Wilcoxon Signed Rank, $P_{Total\ Overlap}$ = 0.0331, $P_{Cell.\ Auto.}$ = 0.5778, $P_{Non\text{-}Cell\ Auto.}$ = 8.825e-06.

Methods-Only References

56. Xiao, C. *et al.* MiR-150 Controls B Cell Differentiation by Targeting the Transcription Factor c-Myb. *Cell* **131,** 146–159 (2007).

57. Boer, E. de *et al.* Efficient biotinylation and single-step purification of tagged transcription factors in mammalian cells and transgenic mice. *Proc Natl Acad Sci USA* **100,** 7480–5 (2003).

58. Driegen, S. *et al.* A generic tool for biotinylation of tagged proteins in transgenic mice. *Transgenic Res* **14,** 477–82 (2005).

59. Greer, C. B. *et al.* Histone Deacetylases Positively Regulate Transcription through the Elongation Machinery. *Cell Rep.* **13,** 1444–1455 (2015).

60. Dobin, A. *et al.* STAR: ultrafast universal RNA-seq aligner. *Bioinformatics* bts635 (2012). doi:10.1093/bioinformatics/bts635

61. Robinson, M. D., McCarthy, D. J. & Smyth, G. K. edgeR: a Bioconductor package for differential expression analysis of digital gene expression data. *Bioinforma. Oxf. Engl.* **26,** 139–140 (2010).

62. Love, M. I., Huber, W. & Anders, S. Moderated estimation of fold change and dispersion for RNA-seq data with DESeq2. *Genome Biol.* **15,** (2014).

63. Andrews, S. Babraham Bioinformatics - FastQC A Quality Control tool for High Throughput Sequence Data. Available at: https://www.bioinformatics.babraham.ac.uk/projects/fastqc/. (Accessed: 28th April 2017)

64. Krueger, F. Babraham Bioinformatics - Trim Galore! Available at: https://www.bioinformatics.babraham.ac.uk/projects/trim_galore/. (Accessed: 28th April 2017)
65. Merico, D., Isserlin, R., Stueker, O., Emili, A. & Bader, G. D. Enrichment Map: A Network-Based Method for Gene-Set Enrichment Visualization and Interpretation. *PLOS ONE* **5,** e13984 (2010).
66. Smoot, M. E., Ono, K., Ruscheinski, J., Wang, P.-L. & Ideker, T. Cytoscape 2.8: new features for data integration and network visualization. *Bioinforma. Oxf. Engl.* **27,** 431–432 (2011).
67. Hart, T., Komori, H. K., LaMere, S., Podshivalova, K. & Salomon, D. R. Finding the active genes in deep RNA-seq gene expression studies. *BMC Genomics* **14,** 778 (2013).
68. R Core Team. *R: A language and environment for statistical computing.* (R Foundation for Statistical Computing, 2014).

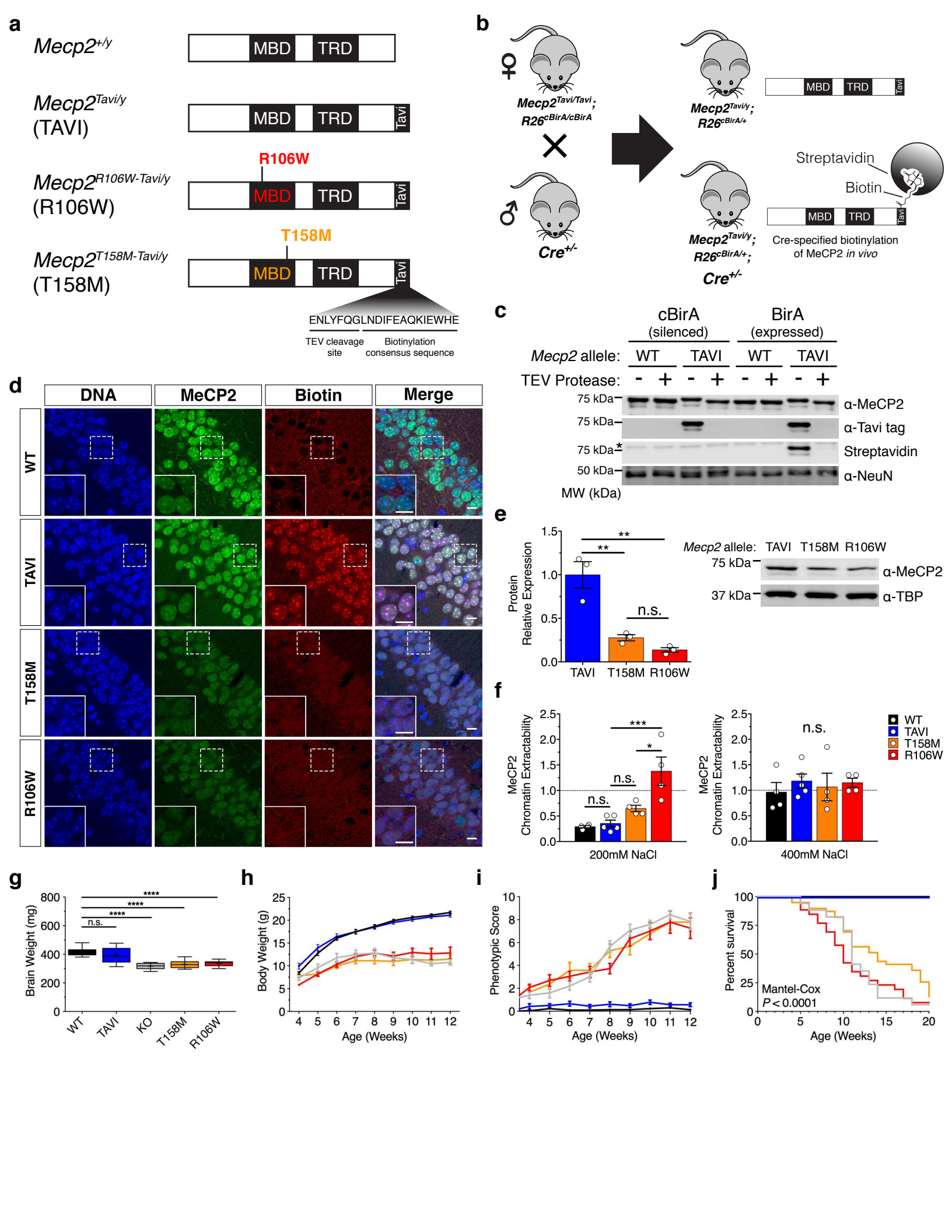
a
Mecp2+/y
MBD
TRD
Mecp2Tavi/y
(TAVI)
Tavi
R106W
Mecp2R106W-Tavi/y
(R106W)
T158M
Mecp2T158M-Tavi/y
(T158M)
ENLYFQGLNDIFEAQKIEWHE
TEV cleavage site
Biotinylation consensus sequence
b
Mecp2Tavi/Tavi; R26cBirA/cBirA
Cre+/-
Mecp2Tavi/y; R26cBirA/+
Mecp2Tavi/y; R26cBirA/+; Cre+/-
Streptavidin
Biotin
Cre-specified biotinylation of MeCP2 in vivo
c
cBirA (silenced)
BirA (expressed)
Mecp2 allele:
WT
TAVI
TEV Protease:
75 kDa
50 kDa
MW (kDa)
α-MeCP2
α-Tavi tag
Streptavidin
α-NeuN
d
DNA
MeCP2
Biotin
Merge
WT
TAVI
T158M
R106W
e
Protein Relative Expression
n.s.
Mecp2 allele:
TAVI
T158M
R106W
37 kDa
α-TBP
f
MeCP2 Chromatin Extractability
200mM NaCl
400mM NaCl
WT
TAVI
T158M
R106W
g
Brain Weight (mg)
KO
h
Body Weight (g)
Age (Weeks)
i
Phenotypic Score
j
Percent survival
Mantel-Cox
P < 0.0001

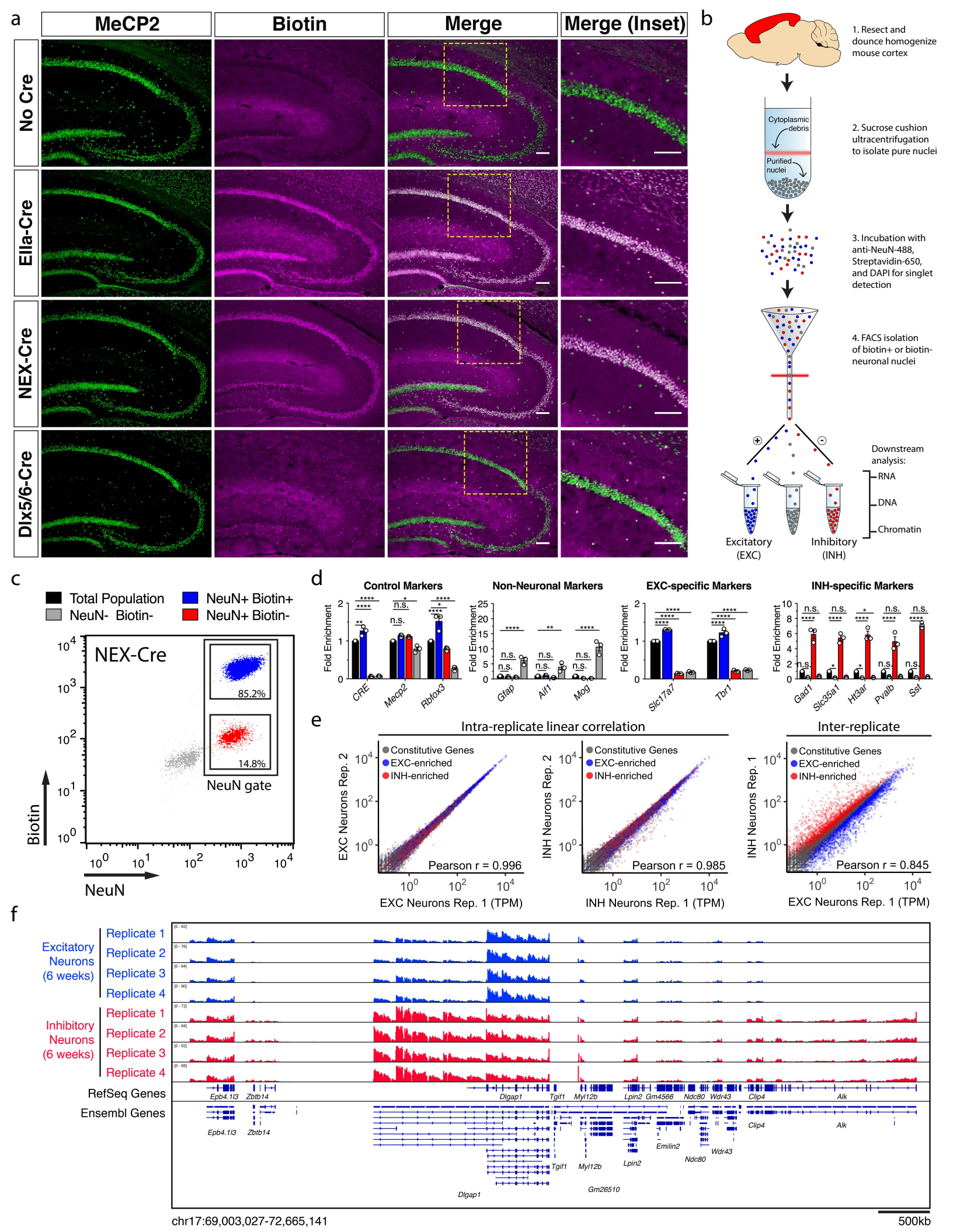
a
MeCP2
Biotin
Merge
Merge (Inset)
No Cre
Ella-Cre
NEX-Cre
Dlx5/6-Cre
b
1. Resect and dounce homogenize mouse cortex
Cytoplasmic debris
Purified nuclei
2. Sucrose cushion ultracentrifugation to isolate pure nuclei
3. Incubation with anti-NeuN-488, Streptavidin-650, and DAPI for singlet detection
4. FACS isolation of biotin+ or biotin- neuronal nuclei
Downstream analysis:
RNA
DNA
Chromatin
Excitatory (EXC)
Inhibitory (INH)
c
Total Population
NeuN- Biotin-
NeuN+ Biotin+
NeuN+ Biotin-
NEX-Cre
85.2%
14.8%
NeuN gate
Biotin
NeuN
d
Control Markers
Non-Neuronal Markers
EXC-specific Markers
INH-specific Markers
Fold Enrichment
CRE
Mecp2
Rbfox3
Gfap
Aif1
Mog
Slc17a7
Tbr1
Gad1
Slc35a1
Hi3ar
Pvalb
Sst
n.s.
e
Intra-replicate linear correlation
Inter-replicate
Constitutive Genes
EXC-enriched
INH-enriched
EXC Neurons Rep. 2
INH Neurons Rep. 2
INH Neurons Rep. 1
Pearson r = 0.996
Pearson r = 0.985
Pearson r = 0.845
EXC Neurons Rep. 1 (TPM)
INH Neurons Rep. 1 (TPM)
f
Excitatory Neurons (6 weeks)
Inhibitory Neurons (6 weeks)
Replicate 1
Replicate 2
Replicate 3
Replicate 4
RefSeq Genes
Ensembl Genes
Epb4.1l3
Zbtb14
Dlgap1
Tgif1
Myl12b
Lpin2
Gm4566
Ndc80
Wdr43
Clip4
Alk
Emilin2
Gm26510
chr17:69,003,027-72,665,141
500kb

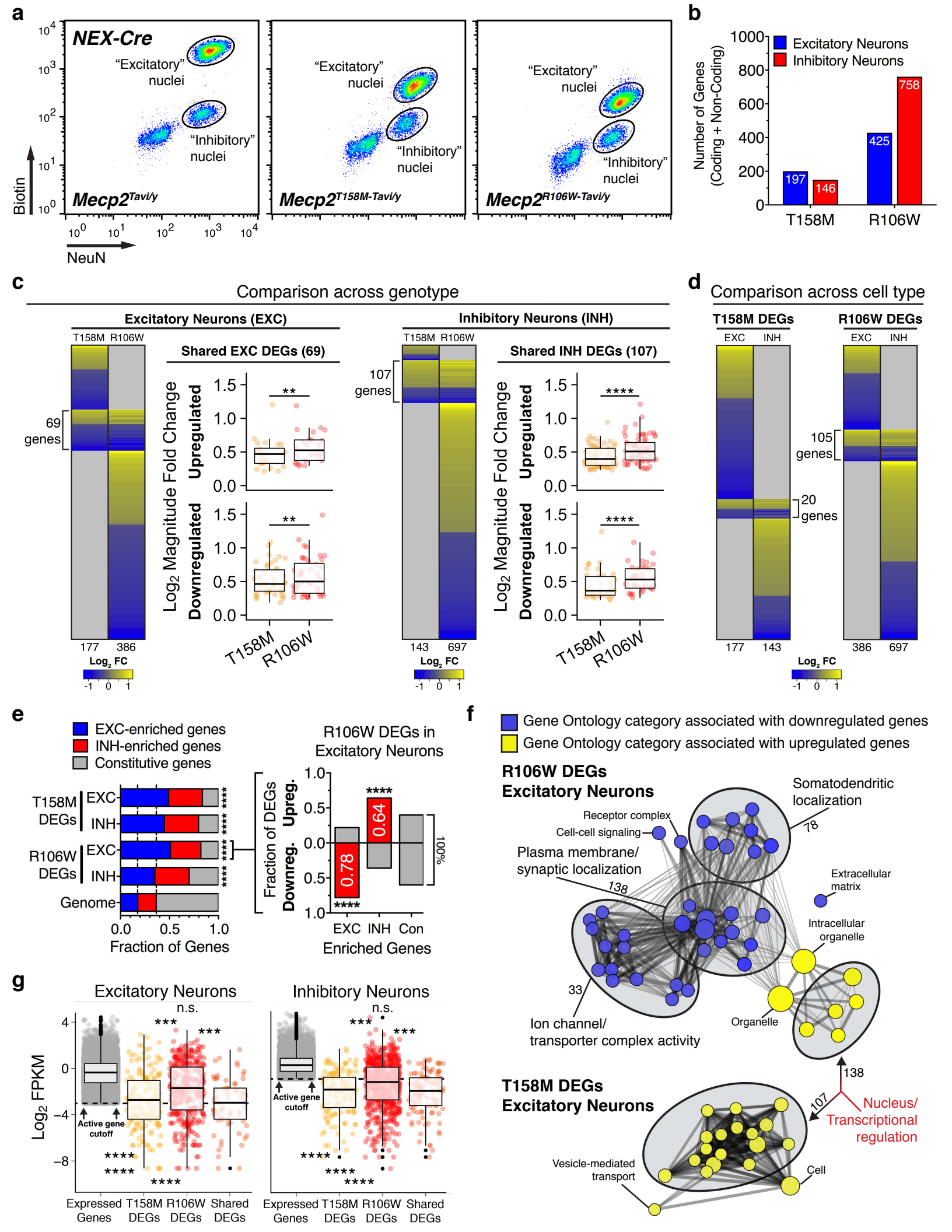
a
NEX-Cre
"Excitatory" nuclei
"Inhibitory" nuclei
Mecp2Tavi/y
Mecp2T158M-Tavi/y
Mecp2R106W-Tavi/y
Biotin
NeuN
b
Excitatory Neurons
Inhibitory Neurons
Number of Genes (Coding + Non-Coding)
197
146
425
758
T158M
R106W
c
Comparison across genotype
Excitatory Neurons (EXC)
Inhibitory Neurons (INH)
Shared EXC DEGs (69)
Shared INH DEGs (107)
69 genes
107 genes
Upregulated
Downregulated
Log2 Magnitude Fold Change
Log2 FC
d
Comparison across cell type
T158M DEGs
R106W DEGs
EXC
INH
105 genes
20 genes
e
EXC-enriched genes
INH-enriched genes
Constitutive genes
T158M DEGs
R106W DEGs
Genome
Fraction of Genes
R106W DEGs in Excitatory Neurons
Fraction of DEGs
Upreg.
Downreg.
0.64
0.78
100%
Enriched Genes
f
Gene Ontology category associated with downregulated genes
Gene Ontology category associated with upregulated genes
R106W DEGs Excitatory Neurons
Somatodendritic localization
Receptor complex
Cell-cell signaling
Plasma membrane/ synaptic localization
Extracellular matrix
Intracellular organelle
Ion channel/ transporter complex activity
Organelle
T158M DEGs Excitatory Neurons
Nucleus/ Transcriptional regulation
Vesicle-mediated transport
Cell
g
Excitatory Neurons
Inhibitory Neurons
Log2 FPKM
Active gene cutoff
n.s.
Expressed Genes
T158M DEGs
R106W DEGs
Shared DEGs

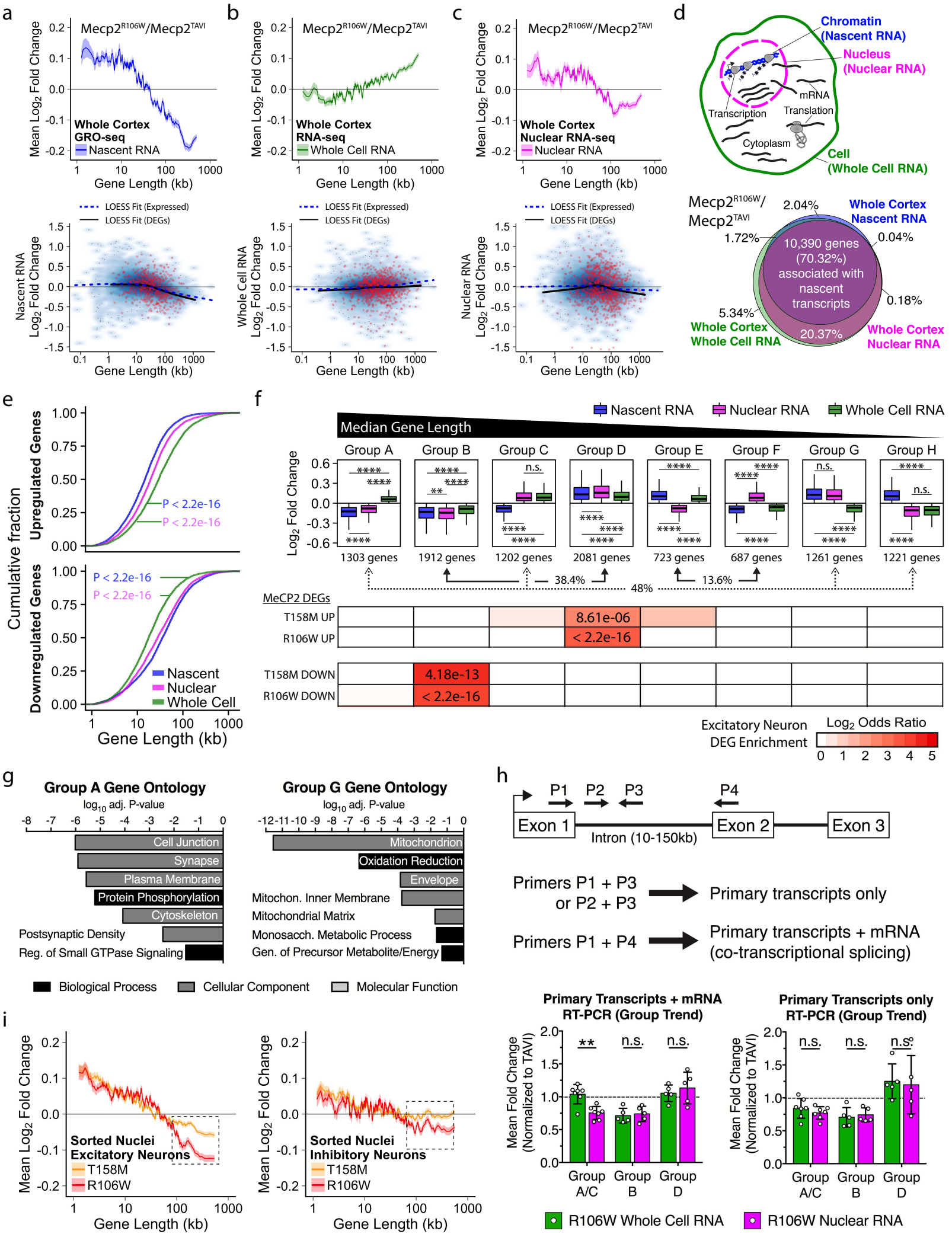
a
b
c
d
Mecp2R106W/Mecp2TAVI
Mean Log2 Fold Change
Gene Length (kb)
Whole Cortex
GRO-seq
Nascent RNA
Whole Cortex
RNA-seq
Whole Cell RNA
Whole Cortex
Nuclear RNA-seq
Nuclear RNA
LOESS Fit (Expressed)
LOESS Fit (DEGs)
Nascent RNA
Log2 Fold Change
Whole Cell RNA
Nuclear RNA
Chromatin
(Nascent RNA)
Nucleus
(Nuclear RNA)
mRNA
Transcription
Translation
Cytoplasm
Cell
(Whole Cell RNA)
Mecp2R106W/
Mecp2TAVI
2.04%
Whole Cortex
Nascent RNA
1.72%
10,390 genes
(70.32%)
associated with
nascent
transcripts
0.04%
0.18%
5.34%
Whole Cortex
Whole Cell RNA
20.37%
Whole Cortex
Nuclear RNA
e
f
Cumulative fraction
Upregulated Genes
Downregulated Genes
P < 2.2e-16
Nascent
Nuclear
Whole Cell
Gene Length (kb)
Nascent RNA
Nuclear RNA
Whole Cell RNA
Median Gene Length
Group A
Group B
Group C
Group D
Group E
Group F
Group G
Group H
Log2 Fold Change
n.s.
1303 genes
1912 genes
1202 genes
2081 genes
723 genes
687 genes
1261 genes
1221 genes
38.4%
48%
13.6%
MeCP2 DEGs
T158M UP
R106W UP
T158M DOWN
R106W DOWN
8.61e-06
< 2.2e-16
4.18e-13
Excitatory Neuron
DEG Enrichment
Log2 Odds Ratio
g
h
Group A Gene Ontology
Group G Gene Ontology
log10 adj. P-value
Cell Junction
Synapse
Plasma Membrane
Protein Phosphorylation
Cytoskeleton
Postsynaptic Density
Reg. of Small GTPase Signaling
Mitochondrion
Oxidation Reduction
Envelope
Mitochon. Inner Membrane
Mitochondrial Matrix
Monosacch. Metabolic Process
Gen. of Precursor Metabolite/Energy
Biological Process
Cellular Component
Molecular Function
P1
P2
P3
P4
Exon 1
Exon 2
Exon 3
Intron (10-150kb)
Primers P1 + P3
or P2 + P3
Primary transcripts only
Primers P1 + P4
Primary transcripts + mRNA
(co-transcriptional splicing)
i
Sorted Nuclei
Excitatory Neurons
Inhibitory Neurons
T158M
R106W
Primary Transcripts + mRNA
RT-PCR (Group Trend)
Primary Transcripts only
RT-PCR (Group Trend)
Mean Fold Change
(Normalized to TAVI)
**
n.s.
Group
A/C
Group
B
Group
D
R106W Whole Cell RNA
R106W Nuclear RNA

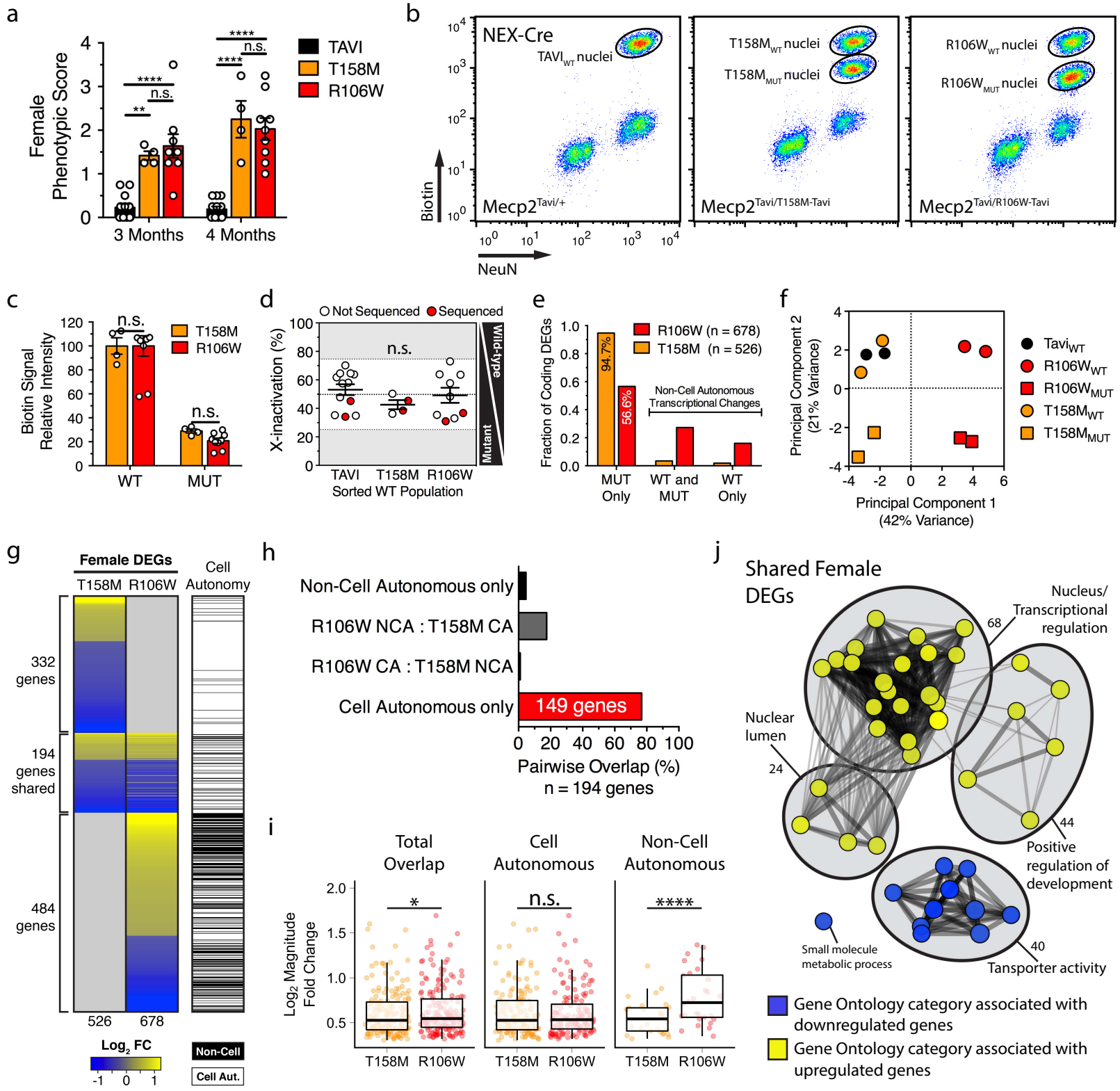
a
Female Phenotypic Score
TAVI
T158M
R106W
3 Months
4 Months
b
NEX-Cre
TAVI$_{WT}$ nuclei
T158M$_{WT}$ nuclei
T158M$_{MUT}$ nuclei
R106W$_{WT}$ nuclei
R106W$_{MUT}$ nuclei
Mecp2$^{Tavi/+}$
Mecp2$^{Tavi/T158M-Tavi}$
Mecp2$^{Tavi/R106W-Tavi}$
Biotin
NeuN
c
Biotin Signal Relative Intensity
WT
MUT
d
Not Sequenced
Sequenced
X-inactivation (%)
Wild-type
Mutant
TAVI
T158M
R106W
Sorted WT Population
e
Fraction of Coding DEGs
R106W (n = 678)
T158M (n = 526)
94.7%
56.6%
Non-Cell Autonomous Transcriptional Changes
MUT Only
WT and MUT
WT Only
f
Principal Component 2 (21% Variance)
Principal Component 1 (42% Variance)
Tavi$_{WT}$
R106W$_{WT}$
R106W$_{MUT}$
T158M$_{WT}$
T158M$_{MUT}$
g
Female DEGs
T158M R106W
Cell Autonomy
332 genes
194 genes shared
484 genes
526
678
Log$_2$ FC
Non-Cell
Cell Aut.
h
Non-Cell Autonomous only
R106W NCA : T158M CA
R106W CA : T158M NCA
Cell Autonomous only
149 genes
Pairwise Overlap (%)
n = 194 genes
i
Total Overlap
Cell Autonomous
Non-Cell Autonomous
Log$_2$ Magnitude Fold Change
T158M R106W
j
Shared Female DEGs
Nucleus/ Transcriptional regulation
Nuclear lumen
Positive regulation of development
Small molecule metabolic process
Tansporter activity
Gene Ontology category associated with downregulated genes
Gene Ontology category associated with upregulated genes